Parameter dependencies of the separatrix density in low triangularity L-mode and H-mode JET-ILW plasmas

B. Lomanowski[1], G. Rubino[2], A. Uccello[3], M. Dunne[4], N. Vianello[5], S. Aleiferis[6], J. Canik[1], I. Carvalho[7], G. Corrigan[8], L. Frassinetti[9], D. Frigione[10], L. Garzotti[8], M. Groth[11], A. Meigs[8], M. Maslov[8], C. Perez von Thun[12], F. Rimini[8], P.A. Schneider[13], G. Sergienko[13], J. Simpson[8,11], D. Van Eester[14], and JET Contributors[*]

[1] Oak Ridge National Laboratory, Oak Ridge, TN 37831-6169, USA
[2] University of Tuscia, DEIM, Via del Paradiso 47, 01100 Viterbo, Italy
[3] Instituto per la Scienza e Tecnologia dei Plasmi, CNR, via Cozzi 53, 20125 Milan, Italy
[4] Max Planck Institut für Plasmaphysik, Garching, Germany
[5] Consorzio RFX (CNR, ENEA, INFN, Università di Padova, Acciaierie Venete SpA), Corso Stati Uniti 4, 35127 Padova, Italy
[6] NCSR 'Demokritos' 153 10, Agia Paraskevi Attikis, Greece
[7] Instituto de Plasmas e Fusão Nuclear, Instituto Superior Técnico, Universidade de Lisboa, Portugal
[8] CCFE, Culham Science Centre, Abingdon OX14 3DB, UK
[9] Fusion Plasma Physics, EES, KTH, SE-10044 Stockholm, Sweden
[10] Unità Tecnica Fusione, ENEA C. R. Frascati, via E. Fermi 45, 00044 Frascati (Roma), Italy
[11] Aalto University, PO Box 14100, FIN-00076 Aalto, Finland
[12] Institute of Plasma Physics and Laser Microfusion (IPPLM), Hery Str 23, 01-497 Warsaw, Poland
[13] Forschungszentrum Jülich GmbH, Institut für Energie- und Klimaforschung, Plasmaphysik, 52425 Jülich, Germany
[14] Laboratory for Plasma Physics Koninklijke Militaire School, Ecole Royale Militaire Renaissancelaan, 30 Avenue de la Renaissance B-1000, Brussels, Belgium

E-mail: lomanowskiba@ornl.gov

Abstract

The midplane electron separatrix density, $n_{e,sep}$, in JET-ILW L-mode and H-mode low triangularity unseeded plasmas exhibits a strong explicit dependence on the averaged outer divertor target electron temperature, $n_{e,sep} \propto \langle T_{e,ot} \rangle^{-1/2}$, arising from parallel pressure balance, as well as on the ratio of the power and momentum volumetric loss factors, $(1\text{-}f_{cooling})/(1\text{-}f_{mom\text{-}loss})$, in line with expectation from the analytic reversed two point model (rev-2PM). Quantifying the influence of the $(1\text{-}f_{cooling})$ and $(1\text{-}f_{mom\text{-}loss})$ loss factors on $n_{e,sep}$ has been enabled by measurement estimates of these quantities from L-mode density ramps in the outer horizontal, VH(C), and vertical target, VV, divertor configurations. Rev-2PM $n_{e,sep}$ estimates from the extended H-mode and more limited L-mode datasets are recovered to within ±25% of the measurements, with a scaling factor applied to account for use of $\langle T_{e,ot} \rangle$, an averaged quantity, rather than flux tube resolved target values. Both the $(1\text{-}f_{cooling})$ and $(1\text{-}f_{mom\text{-}loss})$ trends and recovery of $n_{e,sep}$ using the rev-2PM formatting are reproduced in EDGE2D-EIRENE L-mode-like and H-mode-like density scan simulations.

The general lack of a divertor configuration effect in the JET-ILW $n_{e,sep}$ trends can be attributed to a significant influence of main chamber recycling (MCR), which has been shown in the EDGE2D-EIRENE results to moderate $n_{e,sep}$ with respect to changes in divertor neutral leakage imposed by changes in the divertor configuration. The unified $n_{e,sep}$ vs $\langle T_{e,ot} \rangle$ trends can, however, be broken if large modifications to the divertor geometry (e.g., complete removal of the outer divertor baffle structure) are introduced in the model.

Considerably higher inner target density profiles in the VH(C) configuration with reduced clearance to the separatrix do not have a significant effect on the outer midplane $n_{e,sep}$ and $n_{e,ped}$ vs $\langle T_{e,ot}\rangle$ trends. The more pronounced high-field side high density (HFSHD) region formation in the VH(C) configuration does not therefore appear to play a strong role in fueling the outer midplane confined plasma, although conditions at the inner midplane could not be assessed.

1. Introduction

The purpose of this paper is to further elucidate the plasma parameter correlations with the outer target electron temperature in JET with the ITER-like wall (JET-ILW) reported in the companion paper [1], with a focus on the outer midplane separatrix density scaling. The key point from these experimental observations is that changes in global and edge plasma parameters ($H_{98(y,2)}$, dimensioneless collisionality ν^*, core density peaking $n_{e,0}/\langle n_e\rangle$, separatrix density $n_{e,sep}$) with variations in the D_2 fueling rate and divertor configuration are unified into a single trend when mapped to $\langle T_{e,ot}\rangle$, the spatially averaged spectroscopically derived outer target electron temperature. We noted that the remarkably robust $H_{98(y,2)}$ trend with $\langle T_{e,ot}\rangle$ is connected to a strong inverse correlation between $\langle T_{e,ot}\rangle$, $n_{e,sep}$ and ν^* in predominantly neutral beam heated plasmas. Thus the established relationship between ν^*, $n_{e,0}/\langle n_e\rangle$ and core pressure (see [2] and references therein) can be linked directly to changes in the divertor recycling moderated by $\langle T_{e,ot}\rangle$, such that decreasing $\langle T_{e,ot}\rangle$ (increasing $n_{e,sep}$ and ν^*) via additional D_2 fueling leads to a degradation of plasma performance as a consequence of reduced $n_{e,0}/\langle n_e\rangle$, $T_{e,ped}$ and core pressure via electron temperature profile stiffness.

Given the importance of $n_{e,sep}$ as an interface parameter constraining the compatibility between plasma performance and divertor detachment, we focus in the present work on developing a consistent description of the relationship between divertor conditions and gas fuelled (unseeded) edge plasma behavior. We examine the applicability and limitations of reduced models such as the reversed two-point model (rev-2PM) [3] to describe the main physical processes governing the $n_{e,sep}$ scaling. We will address the observed primary dependence of $n_{e,sep}$ on $\langle T_{e,ot}\rangle$ and the apparent lack of divertor configuration dependence in the $n_{e,sep}$, $n_{e,sep}/n_{e,ped}$ and $H_{98(y,2)}$ vs $\langle T_{e,ot}\rangle$ trends shown in [1], which is perhaps surprising/unexpected and counterintuitive given the differences in divertor target inclination and degree of closure.

Recent experimental and modelling studies of divertor geometry on DIII-D [4–6] have shown a clear influence of closure on the particle flux rollover point (onset of particle detachment) mapped to the outer mid-plane (OMP) pedestal and separatrix densities. The geometry differences between the DIII-D lower single null (LSN) open geometry and upper single null (USN) closed and small angle slot (SAS) divertors are more extreme than the range of available LSN divertor configurations on JET-ILW. We will show that the unified $n_{e,sep}$ vs $\langle T_{e,ot}\rangle$ trends can indeed be broken with a sufficiently large change in the divertor geometry, for example by removing the entire outer divertor structure in 2D edge plasma simulations such that the resulting geometry resembles the DIII-D LSN open divertor. In addition, we will infer from measurements and modelling that main-chamber recycling plays a significant role in moderating the influence of the geometry dependent neutral leakage rates from the divertor on the outer midplane $n_{e,sep}$, and discuss the challenges in capturing these effects with the extended rev-2PM.

In ASDEX-Upgrade (AUG), a correlation between p_0, the divertor neutral pressure, and $n_{e,sep}$ has been established empirically giving $n_{e,sep} \propto p_0^{0.31}$. Using the rev-2PM to relate the target ion flux to the recycling neutral flux and p_0, the $n_{e,sep}$ scaling on AUG is developed by merging the unknown volumetric loss factors for power and momentum losses observed to depend mostly on p_0 through a regression analysis of AUG H-mode discharges [7,8]. Similarly, Leonard et al [9] have used the rev-2PM with an explicit dependence on the outer divertor electron temperature instead of the target ion flux, to recover measurements of $n_{e,sep}$ within reasonable agreement over a range of I_p, B_t and P_{NBI} in DIII-D H-modes in a fixed LSN open geometry. A consistent rise in $n_{e,sep}$ was observed with decreasing divertor target electron temperature, measured with the divertor Thomson scattering system (DTS). The $n_{e,sep}$ trends were found to follow the rev-2PM scaling, but only if the volumetric radiated power losses were taken into account (pressure losses were assumed to be small). Thus, given the successful application of the rev-2PM in these previous studies to inform the $n_{e,sep}$ parameter dependencies, we will extend its use in interpreting the experimentally measured $n_{e,sep}$ in JET-ILW leveraging direct measurements of the volumetric momenutm and cooling loss factors. Quantifying these factors is enabled by spectroscopically inferred outer target electron temperature measurements. We will consider the limitations of the rev-2PM in capturing 2D recycling distribution changes via different divertor configurations.

Whereas relatively strong $n_{e,sep}$ dependencies on p_0 and on $\langle T_{e,ot}\rangle^{-1/2}$ are observed on AUG and JET-ILW (see companion paper [1]), respectively, SOLPS4.3 and SOLPS-ITER simulations of ITER baseline scenarios show a rather weak coupling

between $n_{e,sep}$ and divertor neutral pressure. owing to a projected improved compression of the recycled neutrals at the divertor targets [10]. Further numerical studies of ITER early operation phases indicate that the larger divertor size of ITER relative to AUG lead to better confinement of neutrals for equivalent ionization/dissociation mean free paths [11,12]. The larger size of the JET-ILW divertor relative to DIII-D and AUG further motivates the interpretation of the $n_{e,sep}$ trends in JET-ILW supported by measurements and modelling, and is an important step in developing a machine size scaling of the degree of coupling between a dissipative divertor and $n_{e,sep}$.

The paper is organized as follows. Section 2 describes the L-mode and H-mode discharge datasets, as well as the EDGE2D and SOLPS-ITER simulation setups. Section 3 gives an overview of the extended 2PM for $n_{e,sep}$, followed by an analysis of measured and predicted cooling and momentum loss factors, which are important target electron temperature dependent parameters in the $n_{e,sep}$ model. In Section 4 the measured $n_{e,sep}$ trends are recovered with the rev-2PM, and its applicability to JET-ILW divertor configurations and more generally its limitations with respect to large changes in divertor geometry are discussed. In Section 5 the apparent absence of a clear divertor configuration dependence on $n_{e,sep}$ trends when mapped to the outer target electron temperature are further examined utilizing 2D edge plasma simulations. The influence of divertor closure, target inclination, high field side (HFS) high density formation and main chamber recycling on $n_{e,sep}$ are explored, followed by conclusions in Section 6.

2. Methodology

The experimental setup, discharge dataset, and diagnostic methods are presented in [1], including a description of the spatially averaged, outer target spectroscopic measurements of the electron temperature, $\langle T_{e,ot} \rangle$ in different divertor configurations. Briefly, the dataset is comprised of dedicated I_p=2 MA, B_t=2.3 T, P_{NBI}=16 MW, P_{ICRH}=2-3 MW low-δ unseeded H-mode discharges in four different divertor configurations (see Figure 1 in [1]), fuelled primarily by toroidally distributed gas introduction modules located in the divertor. The configuration naming convention based on the position of the inner and outer strike points (ISP and OSP) is as follows: i) VH(C) and VH(D): inner vertical, outer horizontal tile 5 stack C and stack D; ii) VV: inner vertical, outer vertical; iii) CC: inner corner, outer corner; and iv) VC(T6): inner vertical, outer on top of tile 6, which is achieved by sweeping the OSP from the corner to the top of tile 6, with the ISP also being swept from the inner corner onto the inner vertical tile.

An expanded dataset of unseeded low-δ deuterium fueled discharges has also been compiled from the 2019-2020 JET-ILW experimental campaign spanning the range: P_{NBI}=9-25 MW, P_{ICRH}=2-5 MW, I_p=1.5-3.4 MA, B_t=1.7-3.5 T and q_{95}=3-3.4. Inter-ELM OMP edge plasma electron temperature and density profiles were obtained using the high resolution Thomson scattering (HRTS) system [13].

We also carried out dedicated L-mode density ramp discharges in the four divertor configurations to evaluate the quality of the spectroscopic $\langle T_{e,ot} \rangle$ measurements, as well as to facilitate an assessment of the volumetric pressure-momentum and cooling loss trends presented in Section 4. Due to operational constraints and to avoid the L-H threshold in the VH configurations, the heating power variation in these discharges is in the range 1.1-2.5 MW, with I_p=2-2.5 MA and B_t=2.3-2.5 T.

2.1 Edge plasma simulation dataset

To aid in the interpretation of the experimental results presented in [1], we have compiled existing EDGE2D-EIRENE [14] edge plasma simulations from [15,16]. These simulations include low power (P_{in}=2.2-3.8 MW) unseeded density scans in deuterium-only plasmas in the VV and VH(C) divertor configurations, including scans with and without cross-field drifts due to $\mathbf{E} \times \mathbf{B}$ and $\mathbf{B} \times \nabla B$. Details on the simulation setups, including assumptions on prescribed radial transport coefficients corresponding to L-mode-like electron density and temperature profiles at the outer midplane (OMP), can be found in [15,16]. These scans have been extended to include the CC(T6) divertor geometry, which approximates the corner-corner (CC) configuration, but with the outer strike point positioned on top of tile 6 rather than in the outer corner (see Figure **1**). This compromise enables computational convergence of the gridding tool Grid2D with a sufficiently wide SOL to largely capture the e-folding length of the radial density and outer target ion flux profiles, while avoiding modification of the divertor baffle geometry. Additionally, while this geometry does not fully capture the enhanced closure that is a salient feature of the CC configuration, it permits the synthetic spectroscopic evaluation of $\langle T_{e,ot} \rangle$ (see [17,18] for details) since the outer strike point is in view of the spectrometer, as is the case in experiment.

To evaluate the influence of the divertor geometry on neutral leakage from the divertor and main chamber recycling (MCR) (see Sections X and X), we have introduced an additional geometry, CC(T6)-open, in which the outer divertor baffle structure has been removed leading to a wide open divertor geometry (see Figure **1**), qualitatively similar to the DIII-D LSN divertor (e.g., [4]). Cross-field drifts in the CC(T6) and CC(T6)-open density scans were not included.

Although the above simulations sets feature L-mode-like radial transport coefficients and lower input power compared to the H-mode experiment dataset with variation in P_{NBI}=9-25 MW, the ability to resolve drift effects combined with relative flexibility in numerical convergence of the plasma solutions made this dataset more accessible for evaluating trends spanning a wide $n_{\mathrm{e,sep}}$ and $\langle T_{\mathrm{e,ot}} \rangle$ range. To partially test the validity of the trends discussed in Sections 4 and 5 to H-mode scenarios, density scans at P_{in}=14 MW were also carried out for the VH(C) and VV configurations, albeit without cross-field drifts activated. These H-mode-like scans feature lower values of the fixed particle and thermal diffusion coefficients ($D_{\perp}$=0.05-0.15 $\mathrm{m^2/s}$, $\chi_{\mathrm{e,i}}$=0.5 $\mathrm{m^2/s}$) at and near the separatrix, giving rise to a more pronounced transport barrier such that the resulting electron temperature and density profiles are matched to the high-resolution Thomson scattering (HRTS) profiles from the low recycling VV and VH(C) H-mode discharges with P_{NBI}=16 MW and P_{ICRH}=2 MW.

In addition to the EDGE2D-EIRENE density scans, we carried out L-mode-like density scans using the SOLPS-ITER code package [19] using the same set of grids for the VH(C) and VV configurations. The primary purpose of the SOLPS-ITER runs was to take advantage of built-in tools for decomposing the OMP ionization source profile by physical origin of the recycled neutrals, as discussed in Section 6.2. The SOLPS-ITER density scans in VH(C) and VV yielded very similar plasma solutions to the corresponding EDGE2D-EIRENE simulations with the same set of radial transport coefficients and input power, thus giving confidence that the ionization profile decomposition is equally valid for the EDGE2D-EIRENE cases.

A notable limitation in both the L-mode-like and H-mode-like density scans is the assumption of constant radial transport coefficients with increasing $n_{\mathrm{e,sep}}$. This simplistic approach is not consistent with tokamak experiments, where a collisionality dependence on radial particle fluxes has been observed [20], as well as turbulence driven widening of the near SOL electron temperature and density fall-off lengths [21], and the formation of flattened density profiles (density shoulders) in the far SOL [22,23]. A more realistic treatment requires an adjustment of the radial transport coefficients informed by experimental observations, as has been demonstrated in [24] via a self-consistent collisionality dependent modification of $D_{\perp}$ in the SOL of time-dependent EDGE2D density scan simulations, and in [25] by increasing the particle transport in the SOL to more accurately fit experimental data corresponding to different time slices of an AUG L-mode density ramp discharge. Further modelling efforts are needed to incorporate and benchmark such heuristic models to capture the variation in the SOL radial transport coefficients.

3. Extended reversed two-point model (rev-2PM)

The extended Two-point Model (2PM) [26,27] has been widely used for relating the upstream pressure p_{u}, density n_{u} and parallel heat flux $q_{\parallel \mathrm{u}}$, to the downstream target quantities n_{t}, T_{t}, and parallel particle flux $\Gamma_{\parallel \mathrm{t}}$, along the same flux-tube, where the downstream quantities are often treated as the dependent variables and the upstream as the 'driver' quantities. Formulated using momentum and energy conservation equations in the SOL, the extended 2PM includes volumetric loss terms that capture the dissipative processes along flux tubes associated with momentum and cooling losses,

$$(1 - f_{\mathrm{mom-loss}}) p_{\mathrm{u}}^{\mathrm{tot}} = p_{\mathrm{t}}^{\mathrm{tot}}, \tag{1}$$

$$\left(1 - f_{\mathrm{cooling}}\right) q_{\parallel \mathrm{u}} R_{\mathrm{u}} = q_{\parallel \mathrm{t}} R_{\mathrm{t}}, \tag{2}$$

due to neutral-plasma collisional processes, impurity radiation and the net loss of energy and momentum from the flux tube due to cross-field transport. $p^{\mathrm{tot}}=(1+M^2)n_{\mathrm{e}}kT_{\mathrm{e}}(1+\tau/z)$ is the total pressure, and $q_{\parallel \mathrm{t}}=\gamma kT_{\mathrm{e,t}}\Gamma_{\parallel \mathrm{t}}$ the parallel heat flux at the target, where M is the mach number, $\tau=T_{\mathrm{i}}/T_{\mathrm{e}}$, and $\gamma \approx 7$ is the sheath heat transmission coefficient, not including the potential energy contribution from surface ion recombination. The full description of the 2PM and expressions for $T_{\mathrm{e,t}}$, $n_{\mathrm{e,t}}$ and $\Gamma_{\parallel,\mathrm{t}}$ are provided in [3]. Our present focus is on the 'reversed' 2PM expression for the upstream electron density, obtained by rearranging equations 15.b in [3],

$$n_{\mathrm{e,u}} = \left[\frac{\sqrt{8m_{\mathrm{f}}}}{e^{3/2}\gamma}\left(\frac{2\kappa_{0\mathrm{e}}}{7}\right)^{2/7}\right]\left[\frac{q_{\parallel \mathrm{u}}^{5/7}}{T_{\mathrm{e,t}}^{1/2}L^{2/7}}\right][(1+\tau_{\mathrm{u}})^{-1}]\left[\left(\frac{1+\tau_{\mathrm{t}}}{2}\right)^{1/2}\right]\left[\frac{\left(1-f_{\mathrm{cooling}}\right)}{(1-f_{\mathrm{mom-loss}})(1-f_{\mathrm{conv}})^{2/7}}\right]\left[\frac{R_{\mathrm{u}}}{R_{\mathrm{t}}}\right], \tag{3}$$

in which $q_{\parallel \mathrm{u}}$ at the outer mid-plane is assumed to be dominated by Spitzer parallel electron heat conduction, giving

$$T_{\mathrm{e,u}} \approx \left(\frac{7(1-f_{\mathrm{conv}})q_{\parallel u}L}{2\kappa_{0e}}\right)^{2/7}, \tag{4}$$

where $L \approx \pi R q_{95}$ is the connection length, $\tau=T_i/T_e$, and f_{conv} is a correction factor for the convective fraction of $q_{\parallel u}$. Further assuming equal inter-ELM power sharing between the inner and outer divertor targets,

$$q_{\parallel \mathrm{u}} = \frac{1/2P_{SOL}}{A} = \frac{1/2P_{SOL}}{2\pi R\lambda_q}\frac{|B|}{B_p}, \tag{5}$$

where λ_q is the power width, $P_{sol}=P_{in}-P_{rad,core} - dW/dt$, $|B|$ and B_p are the total and poloidal magnetic field at the outer mid-plane, and dW/dt is the time derivative of the plasma stored energy. Due to the large variation in ELM size and frequency covered by the H-mode database, it was not possible to estimate dW/dt in a consistent manner, hence an ELM-averaged estimate of dW/dt was used for the P_{sol} estimate at high ELM frequency.

The power width, λ_q, can be estimated using the ITPA H-mode scaling [28] developed from multi-machine divertor heat flux data from a set of discharges in attached divertor conditions, giving $\lambda_q \propto (R/a)\rho_{s,sol}$, where $\rho_{s,sol}=(m_D T_{sep})^{1/2}/(eB_p)$ is the poloidal ion sound Larmor gyro-radius at the separatrix. This scaling has recently been revisited by Eich *et al* [21] to include high density discharges from AUG reaching the H-mode density limit, leading to a generalized power width scaling $\lambda_q \propto \rho_{s,sol}.(1+2.1\alpha_t^{1.7})$, where $\alpha_t \propto$ is a modified turbulence control parameter closely related to a normalized collisionality. In comparison to the original ITPA λ_q scaling, the power width is shown to be broadened by up to a factor of three at high values of edge density with $\alpha_t \approx 1$.

The impact of this modified λ_q scaling, as well as the τ_t, τ_u and f_{conv} terms in equation 3 and 4 are discussed in Section 5.2. Extension of the $\lambda_q(\alpha_t)$ scaling to JET is more challenging than on AUG as the method depends on high quality spatially resolved outer mid plane T_e and n_e profiles in the SOL, hence no attempt is made here to verify this new scaling on JET. T_i/T_e ratios and the upstream parallel heat flux convective fraction are inferred from the EDGE2D density scans as these quantities are not available from experiment. We therefore proceed with a two-fold approach in applying the rev-2PM in an attempt to recover the measured $n_{e,sep}$:

i) In the simplified treatment, *'rev-2PM-simplified'*, we use the established ITPA H-mode λ_q scaling from [28] to estimate $q_{\parallel u}$ and assume constant $\tau_u = 2$, $\tau_t = 1$, $f_{conv}=0$ on the basis of a lack of measurement capability on JET, or in the case of edge T_i charge-exchange recombination spectroscopy measurements, difficulties in interpretation of the data near the separatrix [ref];

ii) In the detailed treatment, *'rev-2PM-detailed'*, we adopt the modified $\lambda_q(\alpha_t)$ scaling from AUG and infer τ_t, τ_u and f_{conv} from the simulations as approximate functions of $\langle T_{e,ot}\rangle$. The EDGE2D fluid model accounts for thermal equipartition power between ions and electrons and includes kinetic corrections via heat flux limit factors [29], which have been found to be necessary to match exprimental data, for example on Alcator C-Mod, in which detailed measurements of the ion-electron temperature ratio were assessed [30].

Lastly, when utilizing 2PM formatting of edge simulation output, the model is typically applied to individual flux tubes to relate the spatially resolved radial profiles of the upstream driver and target parameters, and thus implicitly assuming that recycled neutrals on each flux tube are ionized on the same flux tube [3]. Moreover, the first SOL flux tube next to the separatrix is usually ignored due to an additional particle, momentum and energy sink associated with cross-field transport into the private flux region (PFR). Due to the challenges associated with obtaining flux tube resolved upstream and target measurements from experiment for the range of divertor configurations considered, we instead apply equation 3 to relate $n_{e,sep}$ to $\langle T_{e,ot}\rangle$ in Section 5 with the expectation that a leading coefficient will be needed to match the measurements as this approach deviates from the way in which the 2PM is typically applied. This same approach is utilized in interpreting the modelling results to maintain consistency between experiment and code comparisons.

4. Volumetric pressure-momentum and cooling losses in the SOL-divertor

From the divertor perspective, the optimal target plasma conditions required for viable divertor operation in DT tokamaks with solid plasma facing components (PFCs) are established based on requirements for i) maintaining the steady-state deposited peak heat flux below acceptable levels, typically quoted as $q_{\perp,peak}=10$ MW/m^2 [references Pitts, and ref therein, section 4]; and ii) suppressing the net erosion of the solid target to prevent a rapid loss of material and thus ensure material survivability over the lifetime of a high duty cycle reactor [ref Stangeby 2018]. Satisfying these constraints leads to divertor plasma conditions

requirements of Te,t=5-10 eV, ne,t=1021 m-3 [ref Stangeby 2018]. Driving down $T_{e,t}$ from values approaching the upstream separatrix temperature (~100-200 eV depending on the power crossing the separatrix) to below 10 eV can be achieved by increasing the fuel species particle inventory in the scrape-off layer (SOL) to promote high-recycling and volumetric power and momentum losses via neutral-plasma interactions, as well as introducing extrinsic impurities to dissipate the majority of the exhaust power isotropically via line radiation. Restricting the present discussion to loss channels via neutral-plasma interactions (see e.g. [31] for a more detailed description of the atomic and molecular processes involved), a primary dependence of the volumetric momentum and power losses on $T_{e,t}$ emerges based on the analysis of multi-machine 2D edge plasma simulations [3], and supported by observations from experiments [32,33]. Hence, whereas the main actuators are the auxiliary heating power and gas puffing rate, $T_{e,t}$ is the basic physics parameter which strongly correlates with the volumetric energy and momentum loss factor trends, which in turn are needed to relate the 'upstream' and 'downstream' quantities in the 2PM in dissipative divertor regimes.

The volumetric pressure loss, $(1\text{-}f_{\text{mom-loss}})$ and cooling loss $(1\text{-}f_{\text{cooling}})$ factors were estimated in L-mode density ramp discharges for the VH(C), VV configurations, and partially for the CC configuration, according to equations 1, 2, and 5, as shown in Figure **2**. Flux tube resolved $T_{e,t}$ estimates were obtained in the VH(C) configuration away from the unresolved peak Te,t near the separatrix by applying a correction factor to the spatially resolved Langmuir probe Te,t measurements (see Figure 2 in [ref Lomanowski NF 2021]) using the spectroscopically measured value of <Te,ot>. The LP spatial resolution is similar to the divertor spectroscopic chords (15-17mm **verify this**), hence the LP derived Te,ot near the strike point can also be considered an averaged value around the OSP, but the LP measurements are susceptible to kinetic distortion effects leading to overestimates of Te,ot [ref Stangeby1995, Horacek]. The overestimation of the LP derived Te,t due to kinetic effects leads to an underestimate of the LP derived ne,t according to ne,t,LP $\propto$ 1/sqrt(Te,t,LP) [ref Wesson, Gunn]. As demonstrated in [ref Lomanowski 2019], a factor $\zeta_{LP}=(\langle T_{e,ot}\rangle_{spec}/\langle T_{e,ot}\rangle_{LP})^{0.5}$ can be introduced to approximately correct for the kinetic distortion effects using the spectroscopically derived $\langle T_{e,ot}\rangle_{spec}$ value, assumed to be a more accurate estimation of the thermal electron temperature near the target OSP. This correction to the LP Te,ot radial profile reconciles differences in the measured ne,t,LP and ne,t,spec from Dδ Stark broadening measurements (e.g., Lomanowski NF 2015), as shown in Figure **3**, lending more confidence in the method, while also preserving j_sat $\propto$ ne*c_s $\propto$ ne*(Te)^0.5, the most reliable observable from Langmuir probes (c_s= is the sound speed at the sheath entrance). Line-integration effects have been shown in [ref Lomanowski 2019, 2020] to lead to somewhat underestimated ne,t,spec values within about a factor of two; however, the tendency for Te,t,spec to overestimate the true Te,t by up to a factor of two largely balances underestimates in ne,t,spec, which improves the accuracy of ptot,t=4*ne,t*Te,t estimates near the OSP, assuming M=1 (i.e., the basic form of the Bohm-Chodura sheath condition) and τ=z=1. The uncorrected and corrected ne,t,LP and Te,t,LP radial profiles are contrasted against the spectroscopically derived radial profiles in Figure **3**. In summary, this integrated measurement technique serves as the basis for flux-tube resolved estimates of momentum and cooling losses away from the strike point in the VH(C) configuration, and overcomes the influence of non-thermal electron distribution in distorting the current-voltage characteristics of Langmuir probes, which has hindered such analyses on JET in previous attempts [e.g., ref Guillemaut]. In the VV and CC configurations, only the averaged spectroscopic $\langle T_{e,ot}\rangle$ values were used due to a lack of spatially resolved measurements.

High-resolution Thomson scattering $T_{e,u}$ and $n_{e,u}$ radial profiles [13] in the edge plasma near the separatrix position were used to estimate upstream electron static pressure. 2D tomographic reconstructions from resistive bolometer cameras [34] were used to estimate $P_{\text{rad-core}}$ and hence $P_{sol} = P_{Ohm} + P_{NBI} - P_{\text{rad-core,}}$ whereas the L-mode power width scaling from [35] (the 'F2' multi-machine scaling) was used to account for the observed λ_q widening with increasing density (decreasing $\langle T_{e,ot}\rangle$), giving $\lambda_q \propto f_{GW}^{0.9}$ for fixed machine parameters, where f_{GW} is the Greenwald density limit fraction [36]. Uncertainties in P_{sol} and hence $q_{\parallel u}$ and inner-outer power sharing asymmetries were addressed with the assumption that at low recycling conditions, $(1\text{-}f_{\text{cooling}})$ ≈1, as the volumetric power loss in the SOL is expected to be small. Similarly, uncertainties in the position of the last closed-flux surface (LCFS) in the radial $T_{e,u}$ and $n_{e,u}$ profiles combined with the absence of upstream fuel ion parallel fluid velocity and $T_{i,u}$ measurements are addressed by assuming $(1\text{-}f_{\text{mom-loss}})\approx(1\text{-}f_{\text{mom-loss,e}})\approx1$ in low recycling conditions with M=0, τ=z=1, such that $p_u^{tot}=2n_e k T_e$. The validity of these assumptions is discussed below based on flux tube resolved comparisons of $(1\text{-}f_{\text{mom-loss}})$ from EDGE2D density scans shown in Figure **4** using the total (static + dynamic) upstream pressure, and electron pressure, with the upstream locations taken at the X-point as well as at the outer mid-plane.

The main observation from the experiment results (Figure **2**) is that the onset of electron pressure-momentum losses occurs at about 3-4 eV for all three divertor configurations, within the limitations of mapping $(1\text{-}f_{\text{mom-loss,e}})$ to $\langle T_{e,ot}\rangle$ for the CC and VV configurations. Below 3 eV, the VV $(1\text{-}f_{\text{mom-loss,e}})$ trend exhibits a steeper fall-off relative to VH(C), while for the CC configuration there are insufficient data points below 3 eV to resolve the pressure losses.

The experiment trends with the assumption of $(1\text{-}f_{\text{mom-loss,e}})\approx1$ in low recycling are in best agreement with the EDGE2D L-mode-like $(1\text{-}f_{\text{mom-loss}})$ total pressure trends with the upstream position taken at the X-point (Figure 4.a), with similar differences

observed between VH(C) and VV configurations. Changing the upstream location from the X-point to the outer mid-plane (OMP) in formatting the EDGE2D output gives only a small increase in (1-$f_{\text{mom-loss}}$), and can be attributed to the divertor configuration influence on poloidal ionization and density distributions, as discussed in Section 6.2. However, significant changes to the pressure loss trends are obtained if only the electron pressure is considered, as shown in Figure **4**.c-d. The influence of T_i on the upstream and target total pressure is further clarified in Figure **5**, which shows τ_u and τ_t as a function of $T_{e,t}$. At high $T_{e,t}$, T_i>T_e upstream, while T_i<T_e at the target. As collisionality in the SOL increases and $T_{e,t}$ decreases, T_e and T_i equilibrate, with τ_t reaching unity at 3 eV while τ_u remains above 1 until $T_{e,t}$=1 eV.

A discrepancy between the experiment and EDGE2D (1-$f_{\text{mom-loss,e}}$) results is therefore apparent, since T_e=T_i is assumed in experiment by necessity due to a lack of information on the ion temperature in the SOL, yet the observed trends are more consistent with the EDGE2D (1-$f_{\text{mom-loss}}$) trends using total pressure, rather than electron pressure. It's possible that the influence of electron and ion temperature equilibration on the pressure loss trends is obscured by reduced sensitivity in the $n_{e,t}$ and $T_{e,t}$ spectroscopic measurements in low recycling conditions, since the quality of these measurements improves at higher $n_{e,t}$ and lower $T_{e,t}$. Further constraints on T_i from experiment are required to make more definitive statements regarding this discrepancy. Activation of drifts in the L-mode-like EDGE2D density VH(C) and VV scans has only a minor impact on the above trends.

In Figure **6**.a the EDGE2D VH(C) and VV momentum losses are interpreted in a manner consistent with the analysis in experiment: flux tube resolved measurements of (1-$f_{\text{mom-loss,e}}$) for the diagnostically optimized VH(C) geometry, while mapping (1-$f_{\text{mom-loss,e}}$) to $\langle T_{e,ot}\rangle$ for the VV configuration with the upstream location at the outer mid-plane. The trends have been normalized to the values at 10 eV for consistency with the experiment trends in **Error! Reference source not found.**, given the statistical and systematic uncertainties in low recycling conditions. Good agreement is obtained between the experiment and EDGE2D (1-$f_{\text{mom-loss,e}}$) trends for the VV configuration, while the EDGE2D VH(C) total pressure (1-$f_{\text{mom-loss}}$) trends are in better agreement with experiment. Nevertheless, the moderately steeper slope for the VV configuration at low $\langle T_{e,ot}\rangle$ persists regardless of the interpretation approach.

Considering next the experiment (1-f_{cooling}) trends shown in Figure **2**.b, these estimates are based on flux tube resolved $T_{e,ot}$ measurements for the VH(C) configuration, whereas $\langle T_{e,ot}\rangle$ is used for the VV configuration, consistent with the (1-$f_{\text{mom-loss,e}}$) interpretation. The (1-f_{cooling}) results show that the onset of volumetric cooling losses occurs at around 10 eV, and, similar to the (1-$f_{\text{mom-loss,e}}$) results, a steeper slope/fall-off is observed in the VV configuration below 5 eV. Cooling loss estimates for the CC configuration were not possible due to insufficient information on $n_{e,t}$ and lack of data at low $T_{e,ot}$. The observed differences between VH(C) and VV are reproduced in the EDGE2D L-mode-like density scans, as shown in Figure **7**, if the results are formatted from the simulation output according to equation 2. Values of (1-fcool)omp>1 in the EDGE2D results reflect the fact that q|| is not divergence free between the outer mid-plane and the X-point. More specifically, the EDGE2D (1-fcool)omp trends are in better agreement with the best fit lines obtained from experiment, if these are scaled by a factor of 2. Normalizing the EDGE2D (1-fcool)omp data in the same manner as the estimates from experiments, such that (1-fcool)omp=1 at high Te,ot, leads to good agreement with the experiment trends. If the cooling losses are calculated taking the upstream position at the X-point instead (Figure **7**.a), the EDGE2D trends are observed to be somewhat steeper compared to the experiment.

Lastly, if the simulation cooling losses are evaluated in a manner consistent with the interpretation of the experiment data (i.e., (1-f_{cooling}) $\propto n_{e,t}T_{e,t}^{3/2}/P_{sol}$, mapping the results to <Te,ot> for the VV configuration, and assuming (1-fcool)=1 at 10 eV), the VH(C) cooling losses are overestimated relative to the actual EDGE2D output in Figure **6**.b as well as the experiment fit, and the difference between VH(C) and VV trends is diminished.

From the above interpretations and code formatting, it's clear that the lack of more complete information from experiment required for evaluating the volumetric pressure-momentum and cooling losses poses a challenge in undertaking meaningful comparisons of the observed trends with simulation results. The selection of upstream location, assumptions on tau_u and tau_t, and the degree of spatial resolution of Te,ot all contribute to modifying the (1-fmom) and (1-fcool) trends, depending on the interpretation approach. Nevertheless, in most of the comparisons, the steeper slope in the (1-fmom) and (1-fcool) trends in the VV geometry is a consistent feature, and is likely attributed to differences in the recycling and ionization patterns and neutral pathways in the vertical target geometry, as discussed in Section 5.2, as well as in [37]. The key point is that the basic functional form and primary $T_{e,ot}$ dependence of the (1-f_{cooling}) and (1-$f_{\text{mom-loss,e}}$) loss factors, and their role in evolving ne,sep according to the rev-2PM formulation (equation 3), relies on accurate measurement of several upstream and target quantities, as discussed above, in order to capture the influence of the (1-f_{cooling})/(1-$f_{\text{mom-loss}}$) ratio on ne,sep.

5. 2PM $n_{e,sep}$ estimates in experiment and EDGE2D simulations

5.1 'rev-2PM-simplified' $n_{e,sep}$ estimates – H-mode dataset

Figure **8**.a shows a comparison between the measured $n_{e,sep}$ results spanning the entire H-mode dataset and $n_{e,sep}$ estimates recovered using equation 3 assuming the *rev-2PM-simplified* treatment (i.e., constant λ_q estimated using the ITPA H-mode scaling, $\tau_i = \tau_u = 1$, $f_{conv} = 0$ and $T_{e,sep}$, and hence the separatrix location, estimated using equation 4). The *rev-2PM-simplified* model recovers the measured $n_{e,sep}$ values reasonably well if a scaling factor of 0.2 is used to account for the use of an averaged target temperature $\langle T_{e,ot} \rangle$ rather than resolving the measurements on an individual flux tube basis, giving a ± 25% uncertainty range with no clear divertor configuration dependence observed within the scatter of the data.

Applying the same interpretation approach to EDGE2D H-mode-like density scans (i.e., using equation 4 to obtain $T_{e,sep}$ and $n_{e,sep}$, and the *rev-2PM-simplified* model to format the simulation output) the comparison between the 'measured' and *rev-2PM-simplified* $n_{e,sep}$ is shown in Figure **8**.b, with a scaling factor of 0.3 applied to the *rev-2PM-simplified* results. There is typically <10 % difference in the EDGE2D results between the actual outer mid-plane $n_{e,sep}$ and the value obtained at the position of $T_{e,sep}$ evaluated using equation 4 since the outer mid-plane radial n_e and T_e experiment profiles used to constrain the radial transport coefficients are already shifted to $T_{e,sep} \approx 100$ eV, which is a reasonable value representative of JET H-mode scenarios. Similar to the experiment results, the *rev-2PM-simplified* $n_{e,sep}$ values are consistently within ±15% of the 'measured' values over the range of density scans for the VV and VH(C) configurations, with only a modest difference between the two divertor configurations. Furthermore, the comparable values of the *rev-2PM-simplified* scaling factors needed to align the linear trends to the experimental results (0.2 in experiment, 0.3 in EDGE2D) reinforce the validity of applying the 2PM in the non-conventional manner by using the target quantity $\langle T_{e,ot} \rangle$ instead of the flux tube resolved $T_{e,t}$.

In formatting the EDGE2D results, there is a moderate sensitivity of the trends in Figure **8**.b to the weighting parameter used in averaging the electron temperature over the outer target, $\langle T_{e,ot} \rangle = \int w(s) T_{e,t}(s) ds / \int w(s) ds$, where s is the distance along the outer target in the common SOL from the OSP outward, and $w(s)$ is either $n_{e,t}$, $n_{e,t}^2$ or j_{sat}. Weighting $T_{e,t}$ by the particle flux or target density approximates the line-integrated spectroscopic measurements, which are weighted by the brightness of the Balmer photo-recombination continuum volumetric emission proportional to n_e^2. For simplicity we use $j_{sat}(s)$ as the weighting parameter in formatting all of the simulation output, recognizing that while the interpretation of $\langle T_{e,ot} \rangle$ as a basis for comparing the experiment data to simulations is not straightforward, consistency in interpreting $\langle T_{e,ot} \rangle$ is more important than the choice of weighting parameter.

The importance of the volumetric loss terms on the *rev-2PM-simplified* $n_{e,sep}$ estimates is also illustrated in Figure **8**, where $n_{e,sep}$ is evaluated with and without the $(1-f_{mom\text{-}loss})$ and $(1-f_{cooling})$ terms, i.e., by setting $f_{mom\text{-}loss} = f_{cooling} = 0$. In doing so, a divergence away from the linear trend is observed at high $n_{e,sep}$, with $\langle T_{e,ot} \rangle < 10$ eV, corresponding to the onset of cooling losses. With the $(1-f_{mom\text{-}loss})$ and $(1-f_{cooling})$ terms included, the radiative and ionization-dissociation energy losses associated with the $(1-f_{cooling})$ term outweigh the momentum losses at low $\langle T_{e,ot} \rangle$. Thus, despite a further decrease in $(1-f_{mom\text{-}loss})$ when $\langle T_{e,ot} \rangle$ is driven down by additional gas fueling, the rise in $n_{e,sep} \propto \langle T_{e,ot} \rangle^{-1/2} [(1-f_{cooling})/(1-f_{mom\text{-}loss})]$ is suppressed at low $\langle T_{e,ot} \rangle$ by the $(1-f_{cooling})$ term.

Since the $\langle T_{e,ot} \rangle^{-1/2}$ term in equation 3 dominates over $[(1-f_{cooling})/(1-f_{mom\text{-}loss})]$ when $\langle T_{e,ot} \rangle > 10$ eV, we can attribute the pronounced reduction in $H_{98(y,2)}$ with rising $n_{e,sep}$ and decreasing $\langle T_{e,ot} \rangle$ from 30 to 10 eV shown in [1] mainly to parallel pressure balance as the target pressure and recycling particle flux increase with additional D_2 fueling. Below 10 eV, the $(1-f_{cooling})/(1-f_{mom\text{-}loss})$ ratio in equation 3 plays a more important role in linking divertor detachment with the upstream $n_{e,sep}$, and, to the extent that neutrals penetrate into the confined plasma in low opacity edge plasma conditions, the pedestal density, $n_{e,ped}$. All of the H-mode discharges in the dataset remain below the H-mode density limit, with additional D_2 fueling required to reach the limit being constrained in JET-ILW by neutral beam reionization hot spots on limiter PFCs occurring in discharges with moderate-to-high neutral beam heating power.

As an aside, supressing $n_{e,sep}$ at low $\langle T_{e,ot} \rangle$ in order to minimize pedestal collisionality requires more pronounced $(1-f_{cooling})$ losses with a higher $\langle T_{e,ot} \rangle$ onset. This can be achieved by promoting radiative dissipation in the divertor with extrinsic impurity seeding such that $f_{cooling} \approx f_{rad,imp}$. However, since both power and momentum loss channels are important, the influence of extrinsic impurity seeding on the variation in the $(1-f_{cooling})/(1-f_{mom\text{-}loss})$ ratio has not been demonstrated. So far, a surprisingly strong correlation between $(1-f_{cooling})$ and $(1-f_{mom\text{-}loss})$ has been observed from edge plasma simulation datasets compiled by Stangeby [3] for scans that include extrinsic seeded impurities. It remains to be seen whether this correlation can be broken, as is the expectation, given that $(1-f_{cooling})$ is in principle freely specifiable with power losses being more spatially distributed over the divertor and SOL whereas momentum losses largely occur in a small region in front of the divertor target.

5.2 'rev-2PM-simplified' $n_{e,sep}$ estimates – L-mode dataset

Applying the *rev-2PM-simplified* treatment to recover $n_{e,sep}$ from the L-mode density ramp discharges and EDGE2D L-mode-like density scan datasets shown in Figure **9** yields approximately similar trends to the H-mode results. Despite moderate scatter

and non-linearity in the experiment data, especially for the VH(C) configuration, the measured $n_{e,sep}$ values are recovered to within ±25%, with modifications to the leading coefficient to align the trends (0.35 in experiment, 0.25 in EDGE2D). Since the ITPA λ_q scaling from [28] was derived from a multi-machine regression of H-mode data, its applicability to the L-mode data is in question. Substituting the D1 L-mode scaling, $\lambda_q \propto I_p^{-0.35} f_{GW}^{0.48}$, from [ref Horacek] has only a modest impact on the trends given the small range in I_p (2-2.5 MA) in the L-mode density ramps, and relatively weak λ_q dependence on f_{GW}. Hence, for the limited L-mode dataset, the choice of λ_q scaling did not significantly change the results.

Despite the high quality measurements of the $(1\text{-}f_{cooling})$ and $(1\text{-}f_{mom\text{-}loss})$ factors for the VH(C) configuration, better agreement to the measured $n_{e,sep}$ in experiment was obtained for the VH(C) configuration by using the VV $(1\text{-}f_{cooling})$ and $(1\text{-}f_{mom\text{-}loss})$ fit coefficients. However, the selection of either the VH(C) or the VV $(1\text{-}f_{cooling})$ and $(1\text{-}f_{mom\text{-}loss})$ fit coefficients has only a moderate impact on the results compared to the *rev-2PM-simplified* $n_{e,sep}$ estimates for which the $(1\text{-}f_{cooling})$ and $(1\text{-}f_{mom\text{-}loss})$ factors are neglected altogether, as also shown in Figure **9**. The impact of these loss terms is clearly more pronounced in the L-mode dataset as the density ramps are not limited by neutral beam reionization hot spots, and can be extended to deep detachment past the outer target ion current rollover point down to very low $\langle T_{e,ot} \rangle$=0.5 eV (see Figure 3 in [1]), by which point the $(1\text{-}f_{cooling})$ and $(1\text{-}f_{mom\text{-}loss})$ factors have decreased by an order of magnitude or more. In this low temperature, pronounced particle detachment regime, the $(1\text{-}f_{cooling})/(1\text{-}f_{mom\text{-}loss})$ ratio is clearly the dominant term suppressing a further rise in $n_{e,sep}$. The relatively linear trends obtained when the volumetric loss terms are included reinforces the fact that the $(1\text{-}f_{cooling})$ and $(1\text{-}f_{mom\text{-}loss})$ estimates are essential for reconciling the measured $n_{e,sep}$, despite the discrepancies within the ±25% data scatter.

For consistency with the interpretation of experiment data, the EDGE2D *rev-2PM-simplified* results were also evaluated using the VV $(1\text{-}f_{cooling})$ and $(1\text{-}f_{mom\text{-}loss})$ fit coefficients obtained from experiment, although, as already mentioned above, the choice of fit coefficients from either the VV or VH(C) $(1\text{-}f_{cooling})$ and $(1\text{-}f_{mom\text{-}loss})$ trends mainly shifts the $n_{e,sep,2PM}$ scaling factor without much influence on the overall trends. The EDGE2D results also include the CC(T6)-open configuration, which corresponds to the wide open divertor geometry with the outer divertor baffles entirely removed. Whereas the differences between the VH(C), VV and CC(T6) $n_{e,sep,2PM}$ EDGE2D trends are relatively small, a markedly steeper trend is obtained for the CC(T6)-open configuration using the same value for the leading coefficient. This steeper trend arises because the same leading coefficient is no longer valid for the hypothetical wide open configuration due to considerably higher neutral leakage and higher $n_{e,sep,}$ as will be shown in section 6. These effects are captured in the 2PM as an increase in the $(1\text{-}f_{cooling})/(1\text{-}f_{mom\text{-}loss})$ ratio when taken at the OMP, mainly caused by a decrease in $(1\text{-}f_{mom\text{-}loss}) \propto n_{e,sep}^{-1}$ at high $\langle T_{e,ot} \rangle$ above the momentum loss onset temperature. Combined with a roughly 15% increase in $\tau_u = T_{i,u}/T_{e,u}$ in the CC(T6)-open configuration due to higher ionization levels at the OMP, an overall correction factor of about 1.5 is obtained in order to align the CC(T6)-open *rev-2PM-simplified* $n_{e,sep}$ results in Figure **9**.b onto the 1:1 trend line.

The above results indicate that: i) the variation in the VV, VH(C) and CC(T6) divertor configurations (including closure and target inclination) is not sufficient to cause significant differences in the $(1\text{-}f_{cooling})/(1\text{-}f_{mom\text{-}loss})$ ratio; and ii) generalizing the rev-2PM to capture large changes in geometry relies on detailed 2D modelling since variations in neutral dynamics and their influence on upstream conditions are encoded in the $(1\text{-}f_{cooling})/(1\text{-}f_{mom\text{-}loss})$ ratio, τ_u, as well as τ_t, and f_{conv}, which are discussed next.

5.2 Capturing additional physics processes with the 'rev-2PM-detailed' model-based approach

The measured $n_{e,sep}$ in both experiment and EDGE2D simulations can be recovered using the *rev-2PM-simplified* treatment reasonably well, despite the fairly simplistic assumptions on $\lambda_q \propto B_p^{-1}$ estimated from the ITPA H-mode scaling in attached conditions, neglecting the convective fraction of the parallel heat flux $q_{\parallel u,conv} = f_{conv} q_{\parallel u}$, and neglecting the τ_u, and τ_t dependence on collisionality. The details of neutral leakage, ionization distributions, modifications to cross-field transport in the SOL and λ_q widening with increasing collisionality are encoded in these terms and the $(1\text{-}f_{cooling})/(1\text{-}f_{mom\text{-}loss})$ ratio.

With the *rev-2PM-detailed* treatment, we attempt to quantify the influence of these additional terms on recovering the measured $n_{e,sep}$ values by utilizing the more recent $\lambda_q(\alpha_t)$ scaling accounting for power width widening, and employing the EDGE2D density scans to *approximate* τ_u, and τ_t due to the lack of $T_{i,t}$ and $T_{i,u}$ measurements in experiment, as well the convective parallel heat flux contribution. We focus on the L-mode-like EDGE2D density scans from [15,16] in VV (P_{in}=2.8 MW) and VH(C) (P_{in}=3.8 MW) configurations, since the plasma solutions in these scans were successfully converged with the drift terms activated, allowing a direct comparison of the influence of drifts and the additional terms in the *rev-2PM-detailed* treatment. Given the primary dependence of $(1\text{-}f_{mom\text{-}loss})$ and $(1\text{-}f_{cooling})$ and $n_{e,sep} \propto T_{e,t}^{-1/2}[(1\text{-}f_{mom\text{-}loss})/(1\text{-}f_{cooling})]$ on $T_{e,t}$ in unseeded deuterium plasmas, we expect the observations from L-mode trends to be applicable to unseeded H-mode plasmas. However, the presence of edge-localized modes (ELMs) in H-modes will likely introduce additional dynamics (e.g., fuel species implantation and desorption on W PFCs [38]) superimposed on the inter-ELM steady-state behaviour, and a stronger cross-

field $E_\theta \times \mathbf{B}$ drift drive due to higher $T_{e,sep}$ approximated by equation 4, since $E_\theta \propto dT/ds$, where E_θ is the poloidal electric field and s is the poloidal distance in the SOL.

Figure **10**.a shows the convective heat flux term $(1\text{-}f_{conv})$ from the EDGE2D L-mode-like VV and VH(C) density scans evaluated at the outer mid-plane in the flux tube adjacent to the separatrix. At $\langle T_{e,ot} \rangle > 10$ eV, with low collisionality in the SOL and the divertor near the sheath-limited regime (small poloidal ∇T_e), convection dominates the upstream SOL parallel heat flow. Activation of drifts further enhances the convective contribution, especially for the VH(C) configuration, with $(1\text{-}f_{conv}) < 0.35$ at $\langle T_{e,ot} \rangle \approx 10$ eV. At $\langle T_{e,ot} \rangle < 10$ eV, parallel electron conduction overtakes convection as the dominant heat flow mechanism, leading to $(1\text{-}f_{conv}) > 0.75$ in the cases without drifts, while a larger convective contribution persists for the cases with drifts. Substituting the $(1\text{-}f_{conv})$ values into equations 3 and 4 yields the rev-2PM results shown in Figure 10.c, which overestimate $n_{e,sep}$ compared to the *rev-2PM-simplified* results shown in Figure 10.b. This is most pronounced for the VH(C) configuration at low densities and with drifts activated, corresponding to the lowest $(1\text{-}f_{conv})$ values. Interestingly, further substitution of τ_u and τ_t values shown in Figure 10.d improves the 2PM $n_{e,sep}$ agreement, except for the lowest $n_{e,sep}$ cases in the VH(C) configuration. These results suggest that the $(1\text{-}f_{conv})$ term is, to a large extent, balanced by the τ_u and τ_t terms in equation 3, at least for the examined cases. It is not clear how general this result is, since there is a configuration dependence on $(1\text{-}f_{conv})$ with the VV results in Figure 10.b-d being less sensitive to the assumptions on f_{conv}, τ_u and τ_t.

An important oversimplification in the above is the assumption of fixed cross-field transport coefficients for the entire range of the density scans. Varying the diffusive radial transport coefficients in a self-consistent manner as a function of collisionality, as was demonstrated in [24], for example, may also influence the $(1\text{-}f_{conv})$, τ_u and τ_t trends, and this needs to be further clarified. We nevertheless proceed to apply the EDGE2D $(1\text{-}f_{conv})$, τ_u and τ_t estimates as functions of $\langle T_{e,ot} \rangle$ to the H-mode experimental dataset, in addition to replacing the ITPA λ_q scaling with the more recent $\lambda_q(\alpha_t)$ scaling from AUG to resolve the power width widening. The comparison of the *rev-2PM-simplified* and *rev-2PM-detailed* H-mode $n_{e,sep}$ results is shown in Figure **11**. The observed decrease in the $n_{e,sep}$ values estimated with the *rev-2PM-detailed* model is mainly attributed to the influence of the convective fraction on the separatrix temperature and therefore the separatrix location and density, since $T_{e,sep} \propto (1\text{-}f_{conv})^{2/7}$. The leading coefficient also needs to be adjusted to align the *rev-2PM-detailed* $n_{e,sep}$ trend with the measurements, but otherwise the differences between the two sets of results are modest. It therefore seems rather fortuitous, as in the EDGE2D results, that the additional terms in the *rev-2PM-detailed* treatment compensate each other in a manner which largely balances their combined contributions in equations 3 and 4. These observations obtained utilizing the *model-based approximations* of the additional terms should not diminish the need to improve T_i measurements in the SOL, to further develop the $\lambda_q(\alpha_t)$ scaling with multi-machine datasets, and to develop a more complete picture of the dependence of the convective parallel heat flux contribution on divertor geometry, machine size and SOL plasma conditions.

6. More detailed EDGE2D assessment of the divertor configuration impact

So far we have not observed any clear evidence of a divertor configuration dependence in the H-mode correlations shown in [ref Lomanowski NF 2022] within measurement uncertainties and also in view of the less reliable $\langle T_{e,ot} \rangle$ estimates in the VV and CC configurations compared to the diagnostically optimized VH(C) configuration. Neither is there a clear divertor configuration dependent trend evident in the rev-2PM $n_{e,sep}$ comparisons for the H-mode and L-mode experiment data and EDGE2D results, except for the hypothetical CC(T6)-open configuration, for which a steeper $n_{e,sep,2PM}$ slope is observed using the same leading coefficient. As noted in section 5.1, an increase in the $(1\text{-}f_{cooling})/(1\text{-}f_{mom\text{-}loss})$ ratio and τ_u reconciles this discrepancy. More generally, a wide open divertor geometry with large neutral leakage and correspondingly higher $n_{e,sep}$ at the outer mid-plane will, by definition (equation 1), decrease the value of $(1\text{-}f_{mom\text{-}loss})$ at $\langle T_{e,ot} \rangle$ above the pressure-momentum loss onset. Hence, although the 2PM is clearly valuable for formatting code results and identifying the physical processes governing $n_{e,sep}$, it is of limited use for capturing the influence of large changes in divertor closure on $n_{e,sep}$ without *a priori* knowledge of the configuration specific $(1\text{-}f_{mom\text{-}loss})$ volumetric losses, and thus $n_{e,sep}$ itself.

A common approach to examining the influence of divertor closure and magnetic configuration on $n_{e,sep}$ is to compare the onset of particle detachment (i.e., the rollover point of the total outer target ion current, $I_{div,ot}$) as a function of $n_{e,sep}$ (or $n_{e,ped}$), since $n_{e,sep}$ is typically considered to be the upstream driving parameter (e.g., [6,15,39] Fil 2021). Given our present focus on correlations with the target electron temperature, we instead take the 'bottom-up' approach by examining the upstream conditions for a given value of $\langle T_{e,ot} \rangle$, since $n_{e,sep}$ (equation 3) and $(1\text{-}f_{mom\text{-}loss})$ and $(1\text{-}f_{cooling})$ are strong functions of $T_{e,t}$. To isolate the divertor configuration impact as much as possible in the H-mode dataset, Figure **12** shows a subset of the H-mode database $n_{e,sep}$ results for 2 MA, 2.3 T scenarios as a function of Γ_{D2} and $\langle T_{e,ot} \rangle$, with P_{sol} in the range 12-17 MW. Representative lines of best fit to the 2PM (equation 3) are also shown in Figure **12**.b for P_{sol}=12 MW and P_{sol}=17 MW to illustrate the influence of the $(1\text{-}f_{cooling})/(1\text{-}f_{mom\text{-}loss})$ ratio on suppressing the rising $n_{e,sep}$ trend at $\langle T_{e,ot} \rangle < 10$ eV. The $n_{e,sep} \propto P_{sol}^{5/7}$ dependence could not

be clearly resolved within the scatter and uncertainties in this dataset due to the moderate range in P_{sol}. The configuration dependence of the 2MA, 2.3T $n_{e,sep}$ trends with Γ_{D2} are more clearly resolved in Figure **12**.a compared to the results shown in [1] where the entire H-mode dataset was shown over a larger I_p range. In unifying these separate trends by replacing Γ_{D2} with $\langle T_{e,ot}\rangle$, there is some indication of higher $n_{e,sep}$ values for the VH(C) configuration at high $\langle T_{e,ot}\rangle$, which would be consistent with the more open geometry, but the limited data points and the greater likelihood of systematic errors in spectroscopic $\langle T_{e,ot}\rangle$ measurements at high values of electron temperature (> 20 eV) in the different configurations preclude a more meaningful assessment. We therefore turn to the edge plasma simulations to further elucidate the divertor configuration impact on ionization patterns, neutral leakage and the role of main-chamber and divertor recycling on $n_{e,sep}$, given the general correspondence between the EDGE2D and experiment $n_{e,sep,2PM}$ results established in section 5.

Figure **13** shows $n_{e,sep}$ as a function of $\langle T_{e,ot}\rangle$ for the subset of the code results which includes: i) the L-mode-like density scans in VH(C), VV, CC(T6) and CC(T6)-open with P_{sol}=3.5 MW, fixed radial transport coefficients and otherwise identical inputs; and ii) the H-mode-like density scans in VH(C) and VV with P_{sol}=14 MW, fixed radial transport coefficients constrained by experimental outer mid-plane n_e and T_e profiles in low-recycling conditions. The corresponding $n_{e,sep,2PM}$ lines of best fit for each power level are also shown with and without the volumetric cooling loss terms to highlight their importance in recovering the observed trends. While the differences in the radial transport coefficients and input powers between the L-mode-like and H-mode-like density scans give rise to a modest separation in the H-mode-like $n_{e,sep}$ vs $\langle T_{e,ot}\rangle$ trends between the VV and VH(C) configurations, the most significant difference is between the CC(T6)-open configuration and the other geometries in the L-mode like density scans. The CC(T6)-open configuration leads to a 50% increase in $n_{e,sep}$ for the entire $\langle T_{e,ot}\rangle$ range. This result is consistent with the differences in $n_{e,sep,2PM}$ shown in Figure **9**.b, and indicates that large changes in the divertor closure are required to break the unified $n_{e,sep}$ vs $\langle T_{e,ot}\rangle$ trends, or, conversely, that the VH(C), VV, CC(T6) configurations, despite their respective differences in closure and target inclination, lead to similar $n_{e,sep}$ values *when mapped to* $\langle T_{e,ot}\rangle$.

Recasting the EDGE2D $n_{e,sep}$ results into the more familiar $I_{div,ot}$ vs $n_{e,sep}$ trends, as shown in Figure **14**, further illustrates that only the CC(T6)-open divertor configuration leads to a marked increase in $n_{e,sep}$ at the $I_{div,ot}$ rollover point. It is important to note that, while both $\langle T_{e,ot}\rangle$ and $I_{div,ot}$ are useful experimentally derived parameters, the above trends do not capture the influence of target inclination and divertor closure on the details of the spatially resolved target parameters. A critical metric from the perspective of target survivability constraints is the peak heat flux deposited on the target, $q_{dep,t}^{peak}$. In this regard, the vertical target geometry has the beneficial feature of concentrating ionization sources close to the separatrix in the region of largest heat flux [32,39,40]. This effect has been observed in JET-ILW L-mode experiments in VV and VH(C) configurations [41] in which the VH(C) outer target $T_{e,t}$ profile derived from Langmuir probes was found to be much more peaked compared to the VV $T_{e,t}$ profile, although this feature was not reproduced in an H-mode N_2 seeding study aimed at comparing the radiative divertor performance in VV and VH(C) configurations [42]. The influence of neutral pathways on the ionization distribution differences in the VV and VH(C) configurations was examined in more detail in [37] where the observed target T_e profile differences were attributed to the dominant role of reflected recycled neutrals from the HFS on the ionization distribution at the outer divertor separatrix in the VV configuration. Further efforts are needed to validate the target n_e, T_e, j_{sat} and $q_{dep,t}$ profiles predicted by 2D boundary plasma codes, including in the CC(T6) configurations, but such studies are challenging on JET-ILW due to diagnostic limitations and measurement uncertainties, and thus necessitate use of observables such as $\langle T_{e,ot}\rangle$ to constrain and evaluate the rev-2PM $n_{e,sep}$ description.

6.1 Neutral leakage from the divertor

To examine the role of neutral leakage from the divertor to the main-chamber on the outer mid-plane $n_{e,sep}$ we adopt the divertor leakage parameter (DLP) introduced in [6]. The DLP is defined as the ratio of the number of neutral particles escaping the divertor to the number of neutral particles born in the divertor, and is shown in Figure **13**.b as a function of $\langle T_{e,ot}\rangle$ for the L-mode-like EDGE2D dataset. For each configuration, the DLP trends are characterized by an initial decrease in the escaping neutrals with decreasing $\langle T_{e,ot}\rangle$, followed by a reversal and eventual increase at low $\langle T_{e,ot}\rangle$. The VV and CC(T6) configurations exhibit similarly low levels (5-15%) of neutral leakage compared to the VH(C) and CC(T6)-open configurations, which show a factor of 2-4 increase in the DLP. Despite similar DLP trends and values for the VH(C) and CC(T6)-open cases, the 50% difference in their respective $n_{e,sep}$ values suggests that the DLP by itself cannot explain the $n_{e,sep}$ vs $\langle T_{e,ot}\rangle$ trends in Figure **13**.a. (Change to % units in the DLP figure).

The LFS ionization distributions in the horizontal target configurations (VH(C), CC(T6) and CC(T6)-open), as shown in **Error! Reference source not found.** for equal values of $\langle T_{e,ot}\rangle$=10 eV, are characterized by an ionization region which, for the moderately open VH(C) and wide open CC(T6)-open configurations, extends into the outer SOL and above the X-point. In the CC(T6)-open configuration, the LFS ionization region extends to the outer mid-plane, similar to the DIII-D open configuration

described in [6], while the presence of the outboard divertor baffle structure in the CC(T6) geometry, and to a lesser extent in the VH(C) geometry, obstructs recycled neutrals from spreading further upward into the main-chamber SOL. Hence, although the DLP trends and values are similar for the VH(C) and CC(T6)-open configurations, the larger extended ionization region in the CC(T6)-open case gives rise to a significantly higher $n_{e,sep}$ at the outer mid-plane. On the other hand, the ionization distribution in the VV geometry is significantly more concentrated near the inner and outer divertor legs along the separatrix, with comparatively little ionization extending above the X-point.

6.2 Influence of main chamber recycling

A significant contribution to the neutral flux at the outer mid-plane region in the EDGE2D and SOLPS simulations is attributed to main chamber recycling (MCR) of fuel species on the Be wall, for which a recycling coefficient of 1 is used in the model for ions and atomic neutrals. To further isolate the impact of the divertor configuration on $n_{e,sep}$, the L-mode-like EDGE2D density scans were repeated with recycling of the fuel species ions on the main chamber Be wall turned off – i.e. modifying the recycling coefficient from 1 to 0 on the Be main chamber wall. Recycling parameters on the divertor W surfaces and the pumping surfaces in the divertor corners were not modified. Such a setup represents an extreme case of recycling suppression on the vessel walls achieved in experiments using, for example, lithium coatings, which have been shown to reduce the recycling coefficient by ~20% [43]. Such active recycling control strategies are not used in JET-ILW, and hence turning off MC recycling in EDGE2D simulations is only intended to aid understanding.

The outer mid-plane $n_{e,sep}$ vs $\langle T_{e,ot} \rangle$ trends for the four divertor configurations with and without MCR are shown in Figure **16**. Excluding MCR leads to: i) up to a factor of two overall reduction in $n_{e,sep}$ relative to results with MC recycling activated; and ii) a clear dependence on the divertor configuration, with $n_{e,sep}$ in the open VH(C) and CC(T6)-open configurations about 40% higher than in the more closed CC(T6) geometry, with the VV $n_{e,sep}$ trend spanning values in between the open and closed horizontal configurations. These simulation results suggest that the MCR could have a moderating effect on the differences in the $n_{e,sep}$ vs $\langle T_{e,ot} \rangle$ trends imposed by the variation in divertor recycling patterns and ionization distributions. For instance, increasing closure has a clear influence on reducing the divertor recycling contribution to $n_{e,sep}$ in the VH(C) vs CC(T6) trends with MCR turned off, yet this benefit appears to be diminished in simulations with MCR turned on, at least when mapping $n_{e,sep}$ to $\langle T_{e,ot} \rangle$. Also, despite virtually identical trends for the VH(C) and CC(T6)-open results with MCR turned off, the larger extent of the ionization region in the LFS SOL (Figure **15**) clearly enhances the MCR at the outer mid-plane, resulting in an overall increase in $n_{e,sep}$ by 40-50%. The contrast between the simulations with and without MCR is also illustrated in the poloidal distribution of the radial flux of neutrals through the separatrix shown in Figure **17**. In the absence of MCR, the separatrix and confined plasma regions are fuelled entirely near the X-point region, with the neutral fluxes being more pronounced in the outer horizontal target VH(C) and CC(T6)-open configurations. Moreover, the absence of large neutral fluxes at the OMP due to MCR leads to $n_{e,sep}$ vs $\langle T_{e,ot} \rangle$ trends that are consistent with the DLP neutral leakage trends shown in Figure **13**.b, in which enhanced closure and vertical target orientation have a pronounced effect in reducing $n_{e,sep}$ for the same $\langle T_{e,ot} \rangle$ values. Since these configuration dependent $n_{e,sep}$ trends are not observed in experiment (Figure **12**.b), we infer that a significant contribution to $n_{e,sep}$ arising from MCR is more consistent with the measurements.

The above analysis does not provide information on the composition of the MCR particle fluxes, which can be attributed to a combination of thermal release of neutrals from the recycled radial plasma flux, reflected charge exchange neutrals, reflected ballistic neutrals which originate in the LFS or HFS divertor, as well as volume recombination of ions. The extent to which the recycled neutrals from divertor targets contribute to the OMP ionization profile depends on the geometric screening/baffling, as well as the physical size of the divertor and the ionization mean-free path for a given plasma solution. In a recent SOLPS-ITER numerical study of an ASDEX-Upgrade L-mode density ramp discharge, Zito et al [25] showed that the dominant contribution to the OMP ionization profile is attributed to the neutral flux originating from recycling at the outer and inner divertor, whereas the MCR component was shown to be small. As acknowledged in the study, these results contrast with an earlier study on the far SOL density shoulder formation by Lunt et al [44], in which a different modelling package was used, EMC3-EIRENE, featuring a computational grid which extends up to the physical wall. The uncertainty in the composition of the MCR flux could therefore be linked to the grid limitations in code packages such as SOLPS and EDGE2D, in which the computational grids do not extend fully to the wall surfaces.

The physical size of the divertor, and the overall neutral compression for a given divertor geometry, also likely plays an important role in determining the magnitude of the target recycled neutrals contribution to the OMP plasma fueling, as demonstrated in SOLPS-ITER simulations of a standard and scaled down (1/3 size) versions of the ITER geometry [ref JS Park APS 2019, and 2021 paper]. In the full size ITER simulations, the large divertor size leads to high neutral compression and decoupling of the divertor neutral pressure from $n_{e,sep}$, such that $n_{e,sep}$ effectively saturates as the neutral pressure is increased in a gas throughput scan. Conversely, for the scaled down ITER simulations with a size similar to ASDEX-Upgrade, $n_{e,sep}$ and

the ionization fraction in the main chamber rises with the divertor neutral pressure. However, the influence of the radial plasma flux from MCR on $n_{e,sep}$ is not clearly identified in the study, since a decomposition of the type carried out in [25] was not attempted.

Following the methodology in [25], we carried out a similar decomposition of the outer mid-plane ionization profile, shown in Figure **18**, using the SOLPS-ITER L-mode-like cases in JET-ILW VH(C) and VV configurations. In contrast to the findings in the ASDEX-Upgrade SOLPS-ITER simulations, the JET-ILW results indicate that the dominant ionization contribution is from main-chamber recycling for the entire range of the density scan, whereas the contributions from the inner and outer divertor recycling are found to be two orders of magnitude smaller. The sensitivity of these results with respect to changes in the outer SOL radial transport coefficients, and influence of the grid extension to the vessel walls were not evaluated and require further study as these effects are likely to have a significant influence on the MCR magnitude. Additionally, the toroidally discrete JET-ILW HFS and LFS limiters and their influence on the poloidally averaged MCR characteristics is also neglected in the 2D edge codes. Nevertheless, assuming that the dominance of MCR contribution from the radial plasma flux on the OMP ionization profile is not invalidated by transport and grid extension modifications, the small contribution to the OMP ionization profile from ballistic neutrals recycled in the divertor would be consistent with the larger size of JET, and hence increased neutral compression, in accordance with the full scale and AUG-sized ITER simulations in [ref JS Park].

Although SOLPS-ITER simulations of the CC(T6)-open configuration were not carried out, it is also reasonable to assume that the considerably more open geometry, and the 50% increase in $n_{e,sep}$ relative to the VH(C) configuration, gives rise to a larger contribution from outer divertor recycled neutrals, which have a more direct path through the cold outer SOL plasma to the OMP region compared to the other configurations.

Measurements of the MCR magnitude and outer midplane ionization profiles from, for example, spatially resolved main chamber D_α emission from tangentially viewing filtered cameras, could provide important modelling constraints. Inversion and interpretation challenges in the analysis of such measurements due to wall reflections and toroidally discrete limiters on JET are being currently addressed but are outside the scope of the present study. The impact of LFS ballooning transport assumptions, shown to be significant in moderating the neutral influx into the confined plasma region [ref Mordijck report, not paper], has also been neglected in the EDGE2D and SOLPS-ITER modelling. Further studies incorporating the above considerations are needed to more fully evaluate the dependence of $n_{e,sep}$ trends on machine size and divertor geometry.

6.3 Influence of the inner divertor conditions

In the foregoing analysis we have so far ignored the conditions at the inner target and how these may be correlated with $\langle T_{e,ot} \rangle$ and $n_{e,sep}$. From a practical standpoint, the inner target is relatively poorly diagnosed compared to the outer target, particularly due to a lack of spectroscopic $\langle T_{e,it} \rangle$ measurements. From the modelling perspective, the inner target conditions are also more sensitive to drift effects [17,45,46] when $B \times \nabla B$ is directed towards the divertor, as is the case for JET-ILW discharges.

The formation of a high-field side high density region (HFSHD) observed on ASDEX-Upgrade [47–49] has been linked to changes in the fueling of the confined plasma and the neutral particle source distribution in an interpretive SOLPS 5.0 modelling study by Reimold et al [50]. The presence of the HFSHD region was found to change the poloidal asymmetry of the IMP and OMP plasma profiles, and lead to changes in the balance of the inward and outward directed drift-driven particle flows across the separatrix, thus modifying the ionization distribution and flow patterns in the SOL. The changes in the confined plasma fueling due to the presence of the HFSHD region have potential implications on plasma performance as well [49,51], with a strong correlation observed between the reduction of the HFSHD front and improvement in plasma confinement, thought to be linked to radial shifts in the pedestal density profile. Observations of the formation of the HFSHD region on JET-ILW have also been reported by Potzel et al [49] in H-mode discharges with sufficiently high heating power using inner divertor spectroscopic D_δ Stark broadening electron density measurements in the VV configuration. However, a detailed interpretive modelling study has not been attempted on JET-ILW to elucidate the influence of the HFSHD region on the ionization distribution, separatrix and confined plasma fueling, made even more challenging given the lack of IMP plasma profile information and neutral pressure gauges in the JET vessel in contrast to the relatively better diagnosed inner SOL region in ASDEX-Upgrade.

The present study provides additional insight into the role of the formation of the HFSHD region on fueling the separatrix and confined plasma and implications on plasma performance, mainly by focusing on contrasting the magnitude and extent of the HFSHD region in the VV and VH(C) configurations. Although the ISP in these configurations is in a similar position on the inner vertical target (tile 3), the clearance between the inner divertor shoulder tile and the separatrix in the VH(C) configuration is less than half of that in the VV configuration (8 cm vs 20 cm, see Figure **19**.a), thus increasing the proximity of the HFSHD region which could potentially lead to enhanced radial plasma fluxes into the confined region. If, following the

conclusions of the ASDEX-Upgrade study in [50], the HFSHD formation plays a significant role in modifying the ionization distribution, flow patterns, and balance of drift-driven radial fluxes and hence the poloidal fueling profile in JET-ILW, we should expect the proximity of the HFSHD structure to the confined plasma, which depends on the divertor configuration, to also modify $n_{e,sep}$, $n_{e,ped}$, $p_{e,ped}$ and global confinement trends.

The extent of HFS-LFS divertor plasma coupling must also be considered in examining the influence of the HFSHD on the upstream parameter trends mapped to $\langle T_{e,ot} \rangle$. In looking at the different pathways of recycled neutrals in the JET-ILW VH(C) configuration, Moulton et al [37] found that the outer divertor ionization distribution was largely independent of the influence of neutrals originating in the inner divertor, whereas the contribution of the inner divertor neutrals to the ionization source near the outer divertor leg in the VV configuration was shown to be significant, but less so away from the sepatarix. Hence, this numerical study suggests that while in the VH(C) configuration $\langle T_{e,ot} \rangle$ is likely decoupled from the details of recycling patterns in the inner divertor, the same cannot be said for the VV configuration, in which $\langle T_{e,ot} \rangle$ could be influenced to some degree by the neutral source in the inner divertor. Nevertheless, it is worth comparing the inner density characteristics of the two configurations, as shown in Figure **19**.b at two values of $\langle T_{e,ot} \rangle \approx 25$ and 2 eV. Whereas the $n_{e,it}$ radial profiles are of similar magnitude and spatial distribution at $R_{maj} > 2.4$ m outboard of the ISP, there is a clear increase in $n_{e,it}$ at $R_{maj} < 2.4$ m in the VH(C) configuration, which is physically located above the inner divertor shoulder (tile 1). The presence of this high density feature above the tile 1 baffle/shoulder has been linked to surface overheating and outgassing of fuel species neutrals trapped in Be co-deposits, which tend to accumulate there [52,53]. The reduced clearance to the separatrix in the VH(C) configuration leads to increased heat flux reaching tile 1 during the ELM cycle, increasing the surface temperature and thus providing a transient source of neutrals that desorb from the Be co-deposits. Previous attempts have not been successful in disentangling this effect on the overall poloidal fueling profile due to the differences in pumping efficiency in the different divertor configurations.

Having now resolved the differences in pumping efficiency by unifying the configuration dependent $n_{e,sep}$ trends mapped to $\langle T_{e,ot} \rangle$ instead of Γ_{D2}, we are now in a position to revisit the significance of this outgassing mechanism on the ELM-averaged plasma fueling and performance. Similar to the 2 MA, 2.3 T $n_{e,sep}$ results shown in Figure 12.b, Figure 19.c shows the corresponding OMP $n_{e,ped}$ trends for the VV and VH(C) configurations, further filtering the dataset to discharges with the same heating power (Pnbi=15-16, Picrh=2-3 MW) to isolate for the possible influence of the HFSHD region proximity to the separatrix. A clear increase in the VH(C) outer midplane $n_{e,ped}$ trend is not observed within the scatter of the data, suggesting that the additional neutral source from the transient tile 1 outgassing is not sufficiently large to influence the OMP confined plasma fueling, assuming that the density pedestal structure is strongly influenced by neutral dynamics. Unfortunately, we cannot assess the impact of the VH(C) tile 1 outgassing on the IMP radial plasma profiles as this region is poorly diagnosed on JET.

Modelling the influence of the tile 1 outgassing mechanism on the plasma solution and poloidal fueling profile poses significant challenges due to the transient ELM-induced desorption of the fuel particle source contained in the Be co-deposits. Capturing these mechanisms necessitates more sophisticated time-dependent simulations and modified recycling and reservoir models capturing Be erosion, migration and co-deposition, and surface temperature evolution, features which are currently under development for the SOLPS-ITER package, for example [52].

Although the dynamics of the inner divertor outgassing are not captured in the EDGE2D L-mode-like density scans, the simulations are still useful for examining the influence of drifts on the HFS JET-ILW plasma and poloidal fueling profile, shown to be a critical ingredient in capturing the HFSHD formation and impact on the SOL plasma in ASDEX-Upgrade[50]. In higher heating power discharges the cross-field $E_\theta \times \mathbf{B}$ drift drive will be stronger since $E_\theta \propto dT/ds$ and $T_{e,sep} \geq 100$ eV compared to the low power EDGE2D cases with P_{in}=2.2-3.8 MW and $50 \leq T_{e,sep} \leq 70$ eV. Nevertheless, the L-mode-like low power EDGE2D cases with drifts activated still serve as an instructive example.

Similar to Figure 3 in [ref Reimold NME 2017], Figure **20** shows the poloidal distribution of the radial fluxes crossing the separatrix, including the inward flux of neutrals fueling the confined plasma, as well as the inward/outward radial plasma flux, for the VV and VH(C) density ($\langle T_{e,ot} \rangle$) scans with and without drifts activated. In the cases with drifts activated, the radial plasma flux is composed of both the diffusive component driven by density gradients, and a convective component due to drifts. The changes in the balance of the inward and outward plasma flux due to drift activation discussed in [ref Reimold NME 2017] are reproduced in these EDGE2D simulations, yielding a strong inward plasma flux fueling the plasma near the top of the vessel, and a more outward dominated plasma flux near the X-point on both the LFS and HFS. Apart from the magnitude of the fluxes, which increase with increasing density (or decreasing $\langle T_{e,ot} \rangle$), these poloidal fueling patterns are consistently present in both VV and VH(C) configurations, and over the entire $\langle T_{e,ot} \rangle$ range, albeit using fixed radial transport coefficients. The poloidal distribution and magnitude of the inward neutral fluxes through the separatrix are not found to be sensitive to the activation of drifts. As such, while drifts clearly play an important role in increasing the radial plasma flux contribution to the total confined plasma fueling, there is no indication that the presence of a HFSHD region is necessary for these changes in the

inward and outward drift-driven radial plasma fluxes to manifest. However, a detailed interpretive modelling effort simultaneously reconciling both LFS and HFS SOL and divertor plasma conditions, such as the one presented in [ref Reimold NME 2017], is not attempted here, and is unfortunately hindered by the lack of IMP plasma profiles and neutral pressure gauges, measurements which were critical for constraining the plasma solution and modifications to the radial transport coefficient on the HFS in [Reimold NME 2017]. Despite these shortcomings, combining i) the absence of a clear influence of the VH(C) tile 1 outgassing on the H-mode OMP $n_{e,ped}$ vs <Te,ot> trends from experiment, with ii) observation of a consistent change in the poloidal plasma fueling profile imposed by drift-driven plasma fluxes present at both low and high densities in the VV and VH(C) EDGE2D L-mode-like simulations, there is so far no clear indication that the HFSHD region is playing a significant role in fueling the outer midplane density profiles in JET-ILW discharges.

7. Summary and conclusions

In this report we have characterized the primary drivers for the outer midplane $n_{e,sep}$ and the strong dependence on the outer divertor target electron temperature, thus linking the transport and recycling mechanisms on open field lines to the observed core and pedestal parameter and global confinement correlations with the averaged outer target electron temperature, $\langle T_{e,ot}\rangle$, described in the companion paper [1].

Recognizing the importance of $n_{e,sep}$ as an interface parameter between the SOL-divertor and the confined plasma regions, we have employed the reversed two point model (rev-2PM) to estimate $n_{e,sep}$ with an explicit dependence on $\langle T_{e,ot}\rangle^{-1/2}$ arising from parallel pressure balance, as well as on the ratio of the power and momentum volumetric loss factors, $(1\text{-}f_{cooling})/(1\text{-}f_{mom\text{-}loss})$, which also exhibits a primary dependence on the outer target electron temperature. Quantifying the influence of the $(1\text{-}f_{cooling})$ and $(1\text{-}f_{mom\text{-}loss})$ loss factors on $n_{e,sep}$ has been enabled by measurements of these quantities from L-mode density ramps in the outer horizontal, VH(C), and vertical target, VV, divertor configurations. The measured onset of cooling and momentum losses at $\langle T_{e,ot}\rangle$ =3-10 eV, as well as a moderately steeper falloff in the VV configuration, are generally consistent with EDGE2D L-mode-like density scan simulations. However, the interpretation and post-processing details of the simulation output have a moderate impact on the agreement with the measured $(1\text{-}f_{cooling})$ and $(1\text{-}f_{mom\text{-}loss})$ trends.

In applying the rev-2PM to recover the measured $n_{e,sep}$ trends, two approaches are considered. In the *rev-2PM-simplified* approach the widening of the power width in the near-SOL with increasing collisionality is ignored and instead the ITPA H-mode λ_q scaling is used. The convective contribution to the upstream parallel heat flux, f_{conv}, is also ignored, and the upstream T_i/T_e=2 is assumed to be a constant while at the target T_i is assumed to be equal to T_e. These simplifications are necessary due to a limited set of measurements in the SOL and divertor. The *rev-2PM-simplified* $n_{e,sep}$ estimates for the extended H-mode dataset are recovered to within ±25%, once a scaling factor of 0.2 is applied to account for the fact that $\langle T_{e,ot}\rangle$, an averaged quantity, is used to relate the downstream conditions to the outer midplane $n_{e,sep}$, whereas the 2PM is intended to be applied on a flux tube resolved basis. A similar factor of 0.3 is obtained by following the same *rev-2PM-simplified* interpretation in post-processing EDGE2D H-mode-like density scans in the VH(C) and VV configurations, lending confidence to the rev-2PM in capturing the dominant processes driving $n_{e,sep}$. The impact of f_{conv} and T_i/T_e on recovering $n_{e,sep}$ with the rev-2PM was estimated using the EDGE2D density scans and mapped as approximate functions of $\langle T_{e,ot}\rangle$. These additional terms derived from the simulations were applied in the *rev-2PM-detailed* model in addition to the recently developed collisionality dependent $\lambda_q(\alpha_t)$ scaling from AUG [21]. While each term in isolation was found to be significant, their combined effect was found to have only a modest impact on recovering the measured $n_{e,sep}$ values. Further studies are needed to clarify how general this result is, as f_{conv}, for example, is found to be more pronounced in the VH(C) configuration compared to VV, in line with expectations of higher upstream ionization in more open divertor geometries. The $\lambda_q(\alpha_t)$ scaling derived from an AUG dataset has also not been tested on other machines at the time of writing.

In the H-mode dataset, we observed that the $(1\text{-}f_{cooling})/(1\text{-}f_{mom\text{-}loss})$ ratio in the rev-2PM has only a moderate impact on recovering the measured $n_{e,sep}$ due to operational constraints in reaching deep detachment via increasing D_2 fueling. In the L-mode dataset, however, this ratio as a function of $\langle T_{e,ot}\rangle$ is observed to be critical for reconciling the measured $n_{e,sep}$ for $\langle T_{e,ot}\rangle$ < ~few eV since lower target temperatures and more pronounced detachment were accessed. Hence, in unseeded neutral-plasma interaction dominated detachment with $\langle T_{e,ot}\rangle$ of a few eV, the $(1\text{-}f_{cooling})/(1\text{-}f_{mom\text{-}loss})$ ratio constitutes the dominant $n_{e,sep}$ driving term. Conversely, at $\langle T_{e,ot}\rangle$ > 10 eV, the $n_{e,sep} \propto \langle T_{e,ot}\rangle^{-1/2}$ term dominates, and consequently the pronounced reduction in $H_{98(y,2)}$ with rising $n_{e,sep}$ and decreasing $\langle T_{e,ot}\rangle$ from 30 to 10 eV shown in [1] is mainly attributed to parallel pressure balance as the target pressure and recycling particle flux rise with increasing D_2 fueling rates.

In the H-mode upstream parameter correlations with $\langle T_{e,ot}\rangle$ shown in [1], a clear divertor configuration dependence could not be distinguished. Similarly, the rev-2PM estimates in VV, VH(C) and the outer corner, CC(T6), configurations do not appear to be sensitive to the range of divertor geometries available on JET-ILW. We examined the divertor configuration effect

in more detail using the EDGE2D L-mode-like density scans and observed that MCR is likely playing a significant role in moderating $n_{e,sep}$ to changes in divertor neutral leakage imposed by changes in the divertor configuration. When MCR of fuel species on the Be wall is turned off, the $n_{e,sep}$ trends diverge in a manner consistent with divertor neutral leakage patterns, i.e., increased closure leads to reduced $n_{e,sep}$ for the same $\langle T_{e,ot} \rangle$, and a vertical target orientation is similarly beneficial. Conversely, when MCR is turned on in EDGE2D simulations, $n_{e,sep}$ increases by 40-70%, and the configuration dependent trends are no longer discernible, which is more consistent with the $n_{e,sep}$ measurements in experiment. A decomposition of the midplane ionization profile in like-for-like SOLPS-ITER simulations revealed that the main chamber neutrals originate predominantly from recycled radial plasma flux on the main chamber wall, rather than from the divertor. An additional EDGE2D density scan was carried out using a hypothetical divertor geometry (CC(T6)-open) in which the entire low field side baffle was removed to test the response of the $n_{e,sep}$ trend to a large geometry change. In the CC(T6)-open geometry the combination of large outboard divertor neutral leakage and main chamber recycling leads to a further 40% increase in upstream density relative to the other configurations, thus confirming that a large change to the JET-ILW divertor geometry is needed, beyond the range of available configurations, to break the observed $n_{e,sep}$ vs $\langle T_{e,ot} \rangle$ trends. We note that the spatially resolved details of divertor target parameters including the target heat fluxes, although not examined in this study due to measurement limitations, are expected to be impacted by the target orientation, as shown in numerical studies [16,37].

The lack of divertor configuration dependence in the $n_{e,sep}$ and $n_{e,ped}$ vs $\langle T_{e,ot} \rangle$ trends also suggests that the previously observed formation of the high-field side high density (HFSHD) region does not significantly influence the outer midplane density and confined plasma fueling, despite the large differences in the clearance between the inner divertor and separatrix among the divertor configurations. This clearance is especially narrow in the VH(C) configuration, which leads to a previously observed enhanced ELM-induced particle source from fuel species outgassing from Be co-deposits on top of the inner divertor. If this particle source contributed significantly to the outer SOL and edge plasma fueling on a time-averaged basis, we would expect the outer midplane $n_{e,sep}$ and $n_{e,ped}$ trends to exhibit a divertor configuration dependence, as the pumping efficiency differences preventing such comparisons in the past have now been resolved by mapping the trends to $\langle T_{e,ot} \rangle$ rather than the D_2 fueling rate. The lack of information on the inner midplane plasma profiles precludes further analysis of the outgassing influence on the HFS edge plasma.

Although modelling the transient outgassing physics is outside the scope of this work, we further investigated the role of the inner divertor high density formation by comparing EDGE2D vertical and outer horizontal configuration L-mode-like density scans with drifts activated. The role of drifts has been previously shown in [50] to be crucial for recovering the higher inner divertor density conditions typically observed in experiments with the $\mathbf{B} \times \nabla B$ direction towards the divertor. However, the EDGE2D simulations show that while drift-driven plasma fluxes change the distribution of the poloidal plasma fueling profile considerably, these changes are present in both configurations and also over the entire range of the density scan and are therefore independent from the evolution of the inner divertor density. The assumption of constant radial transport throughout the entire density scans, and the low power conditions amenable to numerical convergence in these drift-activated cases warrant more detailed analysis of these mechanisms.

In future work further application of the rev-2PM analysis to ITER edge plasma simulations as well as multi-machine experiment and simulation datasets could improve understanding of the $n_{e,sep}$ dependence on machine size, the extent of the MCR and divertor baffling influence on $n_{e,sep}$, and the variation of the $(1\text{-}f_{cooling})/(1\text{-}f_{mom\text{-}loss})$ ratio in optimizing highly radiative impurity seeded scenarios as a possible power exhaust solution. Contrasting the divertor neutral pressure based $n_{e,sep}$ model developed on AUG [7] with the target electron temperature based description presented herein would further advance the development of $n_{e,sep}$ scaling from the perspective of both the dominant engineering and physics parameters.

Acknowledgements

This work has been carried out within the framework of the EUROfusion Consortium and has received funding from the Euratom research and training programme 2014–2018 and 2019–2020 under grant agreement No. 633053. The views and opinions expressed herein do not necessarily reflect those of the European Commission. This work was also supported by the US DOE under Contract No. DE-AC05- 00OR22725 with UT-Battelle, LLC.

References

[1] Lomanowski B, Dunne M, Vianello N, Aleiferis S, Brix M, Canik J, Carvalho I S, Frassinetti L, Frigione D, Garzotti L, Groth M, Meigs A, Menmuir S, Maslov M, Pereira T, Perez von Thun C, Reinke M, Refy D, Rimini F, Rubino G, Schneider P A, Sergienko G, Uccello A, Van Eester D and JET Contributors 2022 Experimental study on the role of the target electron temperature as a key parameter linking recycling to

plasma performance in JET-ILW* *Nucl. Fusion* **62** 066030

[2] Frassinetti L, Beurskens M N A, Saarelma S, Boom J E, Delabie E, Flanagan J, Kempenaars M, Giroud C, Lomas P, Meneses L, Maggi C S, Menmuir S, Nunes I, Rimini F, Stefanikova E, Urano H and Verdoolaege G 2017 Global and pedestal confinement and pedestal structure in dimensionless collisionality scans of low-triangularity H-mode plasmas in JET-ILW *Nucl. Fusion* **57** 016012

[3] Stangeby P C 2018 Basic physical processes and reduced models for plasma detachment *Plasma Phys. Control. Fusion* **60** 044022

[4] Moser A L, Leonard A W, McLean A G, Wang H Q and Watkins J G 2019 The effect of divertor closure on detachment onset in DIII-D *Nucl. Mater. Energy* **19** 67–71

[5] Casali L, Covele B M and Guo H Y 2019 The effect of neutrals in the new SAS divertor at DIII-D as modelled by SOLPS *Nucl. Mater. Energy* **19** 537–43

[6] Casali L, Eldon D, Boedo J A, Leonard T and Covele B 2020 Neutral leakage, power dissipation and pedestal fueling in open vs closed divertors *Nucl. Fusion* **60**

[7] Kallenbach A, Sun H J, Eich T, Carralero D, Hobirk J, Scarabosio A and Siccinio M 2018 Parameter dependences of the separatrix density in nitrogen seeded ASDEX Upgrade H-mode discharges *Plasma Phys. Control. Fusion*

[8] Kallenbach A, Bernert M, Dux R, Eich T, Henderson S S, Pütterich T, Reimold F, Rohde V and Sun H J 2019 Neutral pressure and separatrix density related models for seed impurity divertor radiation in ASDEX Upgrade *Nucl. Mater. Energy* **18** 166–74

[9] Leonard A W, McLean A G, Makowski M A and Stangeby P C 2017 Compatibility of separatrix density scaling for divertor detachment with H-mode pedestal operation in DIII-D *Nucl. Fusion* **57** 086033

[10] Pitts R A, Bonnin X, Escourbiac F, Frerichs H, Gunn J P, Hirai T, Kukushkin A S, Kaveeva E, Miller M A, Moulton D, Rozhansky V, Senichenkov I, Sytova E, Schmitz O, Stangeby P C, De Temmerman G, Veselova I and Wiesen S 2019 Physics basis for the first ITER tungsten divertor *Nucl. Mater. Energy* **20** 100696

[11] Park J S, Bonnin X and Pitts R 2019 Assessment of ITER W divertor performance during early operation phases *61st Annual Meeting of the APS Division of Plasma Physics Volume 64, Number 11*

[12] Park J S, Bonnin X and Pitts R 2021 Assessment of ITER divertor performance during early operation phases *Nucl. Fusion* **61**

[13] Pasqualotto R, Nielsen P, Gowers C, Beurskens M, Kempenaars M, Carlstrom T and Johnson D 2004 High resolution Thomson scattering for Joint European Torus (JET) *Review of Scientific Instruments* vol 75 (American Institute of PhysicsAIP) pp 3891–3

[14] Wiesen S 2006 *EDGE2D/EIRENE code interface report*

[15] Groth M, Brezinsek S, Belo P, Beurskens M N A, Brix M, Clever M, Coenen J W, Corrigan C, Eich T, Flanagan J, Guillemaut C, Giroud C, Harting D, Huber A, Jachmich S, Kruezi U, Lawson K D, Lehnen M, Lowry C, Maggi C F, Marsen S, Meigs A G, Pitts R A, Sergienko G, Sieglin B, Silva C, Sirinelli A, Stamp M F, Van Rooij G J and Wiesen S 2013 Impact of carbon and tungsten as divertor materials on the scrape-off layer conditions in JET *Nucl. Fusion* **53**

[16] Groth M, Brezinsek S, Belo P, Brix M, Calabro G, Chankin A, Clever M, Coenen J W, Corrigan G, Drewelow

P, Guillemaut C, Harting D, Huber A, Jachmich S, Järvinen A, Kruezi U, Lawson K D, Lehnen M, Maggi C F, Marchetto C, Marsen S, Maviglia F, Meigs A G, Moulton D, Silva C, Stamp M F and Wiesen S 2015 Divertor plasma conditions and neutral dynamics in horizontal and vertical divertor configurations in JET-ILW low confinement mode plasmas *J. Nucl. Mater.* **463** 471–6

[17] Lomanowski B, Carr M, Field A, Groth M, Jarvinen A E, Lowry C, Meigs A G, Menmuir S, O'Mullane M, Reinke M L, Stavrou C K and Wiesen S 2019 Spectroscopic investigation of N and Ne seeded induced detachment in JET ITER-like wall L-modes combining experiment and EDGE2D modeling *Nucl. Mater. Energy* 100676

[18] Lomanowski B, Groth M, Coffey I, Karhunen J, Maggi C F, Meigs A G, Menmuir S and O'Mullane M 2020 Interpretation of Lyman opacity measurements in JET with the ITER-like wall using a particle balance approach *Plasma Phys. Control. Fusion* **62** 065006

[19] Wiesen S, Reiter D, Kotov V, Baelmans M, Dekeyser W, Kukushkin A S, Lisgo S W, Pitts R A, Rozhansky V, Saibene G, Veselova I and Voskoboynikov S 2015 The new SOLPS-ITER code package *J. Nucl. Mater.* **463** 480–4

[20] LaBombard B, Hughes J W, Mossessian D, Greenwald M, Lipschultz B and Terry J L 2005 Evidence for electromagnetic fluid drift turbulence controlling the edge plasma state in the Alcator C-Mod tokamak *Nucl. Fusion* **45** 1658–75

[21] Eich T, Manz P, Goldston R J, Hennequin P, David P, Faitsch M, Kurzan B, Sieglin B and Wolfrum E 2020 Turbulence driven widening of the near-SOL power width in ASDEX Upgrade H-Mode discharges *Nucl. Fusion* **60**

[22] Carralero D, Madsen J, Artene S A, Bernert M, Birkenmeier G, Eich T, Fuchert G, Laggner F, Naulin V, Manz P, Vianello N and Wolfrum E 2017 A study on the density shoulder formation in the SOL of H-mode plasmas *Nucl. Mater. Energy* **12**

[23] Wynn A, Lipschultz B, Cziegler I, Harrison J, Jaervinen A, Matthews G F, Schmitz J, Tal B, Brix M, Guillemaut C, Frigione D, Huber A, Joffrin E, Kruzei U, Militello F, Nielsen A, Walkden N R and Wiesen S 2018 Investigation into the formation of the scrape-off layer density shoulder in JET ITER-like wall L-mode and H-mode plasmas *Nucl. Fusion* **58** 056001

[24] Wiesen S, Fundamenski W, Wischmeier M, Groth M, Brezinsek S and Naulin V 2011 Relevance of collisionality in the transport model assumptions for divertor detachment multi-fluid modelling on JET *J. Nucl. Mater.* **415** S535–9

[25] Zito A, Wischmeier M, Carralero D, Manz P, Paradela Pérez I and Passoni M 2021 Numerical modelling of an enhanced perpendicular transport regime in the scrape-off layer of ASDEX Upgrade *Plasma Phys. Control. Fusion* **63** 075003

[26] Pitcher C S and Stangeby P C 1997 Experimental divertor physics *Plasma Phys. Control. Fusion* **39** 779–930

[27] Stangeby P C 2000 *The Plasma Boundary of Magnetic Fusion Devices* (Bristol and Philadelphia: Institute of Physics Publishing)

[28] Eich T, Leonard A W, Pitts R A, Fundamenski W, Goldston R J, Gray T K, Herrmann A, Kirk A, Kallenbach A, Kardaun O, Kukushkin A S, LaBombard B, Maingi R, Makowski M A, Scarabosio A, Sieglin B, Terry J and Thornton A 2013 Scaling of the tokamak near the scrape-off layer H-mode power width and implications

for ITER *Nucl. Fusion* **53** 093031

[29] Tskhakaya D, Subba F, Bonnin X, Coster D P, Fundamenski W and Pitts R A 2008 On kinetic effects during parallel transport in the SOL *Contrib. to Plasma Phys.* **48** 89–93

[30] Brunner D, Labombard B, Churchill R M, Hughes J, Lipschultz B, Ochoukov R, Rognlien T D, Theiler C, Walk J, Umansky M V. and Whyte D 2013 An assessment of ion temperature measurements in the boundary of the Alcator C-Mod tokamak and implications for ion fluid heat flux limiters *Plasma Phys. Control. Fusion* **55**

[31] Kotov V, Reiter D, Pitts R A, Jachmich S, Huber A and Coster D P 2008 Numerical modelling of high density JET divertor plasma with the SOLPS4.2 (B2-EIRENE) code *Plasma Phys. Control. Fusion* **50**

[32] Lipschultz B, LaBombard B, Terry J L, Boswell C and Hutchinson I H 2007 Divertor Physics Research on Alcator C-Mod *Fusion Sci. Technol.* **51** 369–89

[33] Paradela Pérez I, Scarabosio A, Groth M, Wischmeier M, Reimold F and Upgrade Team A 2017 SOL parallel momentum loss in ASDEX Upgrade and comparison with SOLPS *Nucl. Mater. Energy* **12** 181–6

[34] Huber A, McCormick K, Andrew P, de Baar M R, Beaumont P, Dalley S, Fink J, Fuchs J C, Fullard K, Fundamenski W, Ingesson L C, Kirnev G, Lomas P, Mast F, Jachmich S, Matthews G F, Mertens P, Meigs A, Philipps V, Rapp J, Saibene G, Sanders S, Sartori R, Stamp M F and Zeidner W 2007 Improved radiation measurements on JET - First results from an upgraded bolometer system *J. Nucl. Mater.* **363**–**365** 365–70

[35] Horacek J, Adamek J, Komm M, Seidl J, Vondracek P, Jardin A, Guillemaut C, Elmore S, Thornton A, Jirakova K, Jaulmes F, Deng G, Gao X, Wang L, Ding R, Brunner D, Labombard B, Olsen J, Rasmussen J J, Nielsen A H, Naulin V, Ezzat M, Camacho K M, Hron M and Matthews G F 2020 Scaling of L-mode heat flux for ITER and COMPASS-U divertors, based on five tokamaks *Nucl. Fusion* **60**

[36] Greenwald M 2002 Density limits in toroidal plasmas Density limits in toroidal plasmas **27**

[37] Moulton D, Corrigan G, Harrison J R and Lipschultz B 2018 Neutral pathways and heat flux widths in vertical- and horizontal-target EDGE2D-EIRENE simulations of JET *Nucl. Fusion* **58** 096029

[38] Brezinsek S, Wiesen S, Harting D, Guillemaut C, Webster A J, Heinola K, Meigs A G, Rack M, Gao Y, Sergienko G, Philipps V, Stamp M F, Jachmich S and Contributors J 2016 Characterisation of the deuterium recycling at the W divertor target plates in JET during steady-state plasma conditions and ELMs *Phys. Scr.* **T167** 014076

[39] Fil A, Lipschultz B, Moulton D, Dudson B D, Février O, Myatra O, Theiler C, Verhaegh K and Wensing M 2020 Separating the roles of magnetic topology and neutral trapping in modifying the detachment threshold for TCV *Plasma Phys. Control. Fusion* **62** 35008

[40] Loarte A 2001 Effects of divertor geometry on tokamak plasmas *Plasma Phys. Control. Fusion* **43** 183–224

[41] Chankina A V., Delabie E, Corrigan G, Maggi C F, Meyer H and Contributors J E T 2017 Possible influence of near SOL plasma on the H-mode power threshold *Nucl. Mater. Energy* **12** 273–7

[42] Jaervinen A E, Brezinsek S, Giroud C, Groth M, Guillemaut C, Belo P, Brix M, Corrigan G, Drewelow P, Harting D, Huber A, Lawson K D, Lipschultz B, Maggi C F, Matthews G F, Meigs A G, Moulton D, Stamp M F and Wiesen S 2016 Impact of divertor geometry on radiative divertor performance in JET H-mode plasmas *Plasma Phys. Control. Fusion* **58**

[43] Canik J M, Sun Z, Hu J S, Zuo G Z, Xu W, Huang M, Wang L, Xu J, Zhang T, Maingi R, Lunsford R, Diallo A, Mansfield D, Osborne T and Tritz K 2018 Active recycling control through lithium injection in EAST *IEEE Trans. Plasma Sci.* **46** 1081–5

[44] Lunt T, Carralero D, Feng Y, Birkenmeier G, Müller H W, Müller S and Wischmeier M 2015 EMC3-Eirene simulations of particle- and energy fluxes to main chamber- and divertor plasma facing components in ASDEX Upgrade compared to experiments *J. Nucl. Mater.* **463** 744–7

[45] Aho-Mantila L, Potzel S, Coster D P, Wischmeier M, Brix M, Fischer R, Marsen S, Meigs A, Müller H W, Scarabosio A, Stamp M F and Brezinsek S 2017 Assessment of SOLPS5.0 divertor solutions with drifts and currents against L-mode experiments in ASDEX Upgrade and JET *Plasma Phys. Control. Fusion* **59** 035003

[46] Jaervinen A E, Allen S L, Eldon D, Fenstermacher M E, Groth M, , D.N. Hill C L, Leonard A W, McLean A G, Porter G D, Rognlien T D, Samuell C M and Wanga H 2018 Impact of Drifts on Divertor Power Exhaust in DIII-D *Nucl. Mater. Energy*

[47] Reimold F, Wischmeier M, Bernert M, Potzel S, Coster D, Bonnin X, Reiter D, Meisl G, Kallenbach A, Aho-Mantila L and Stroth U 2015 Experimental studies and modeling of complete H-mode divertor detachment in ASDEX Upgrade *J. Nucl. Mater.* **463** 128–34

[48] Potzel S, Wischmeier M, Bernert M, Dux R, Müller H W and Scarabosio A 2014 A new experimental classification of divertor detachment in ASDEX Upgrade *Nucl. Fusion* **54**

[49] Potzel S, Wischmeier M, Bernert M, Dux R, Reimold F, Scarabosio A, Brezinsek S, Clever M, Huber A, Meigs A and Stamp M 2015 Formation of the high density front in the inner far SOL at ASDEX Upgrade and JET *J. Nucl. Mater.* **463** 541–5

[50] Reimold F, Wischmeier M, Potzel S, Guimarais L, Reiter D, Bernert M, Dunne M and Lunt T 2017 The high field side high density region in SOLPS-modeling of nitrogen-seeded H-modes in ASDEX Upgrade *Nucl. Mater. Energy* **12**

[51] Schneider P A, Bustos A, Hennequin P, Ryter F, Bernert M, Cavedon M, Dunne M G, Fischer R, Görler T, Happel T, Igochine V, Kurzan B, Lebschy A, McDermott R M, Morel P and Willensdorfer M 2017 Explaining the isotope effect on heat transport in L-mode with the collisional electron-ion energy exchange *Nucl. Fusion* **57** 066003

[52] Wiesen S, Groth M, Wischmeier M, Brezinsek S, Jarvinen A, Reimold F and Aho-Mantila L 2017 Plasma edge and plasma-wall interaction modelling: Lessons learned from metallic devices *Nucl. Mater. Energy* **12**

[53] De La Cal E, Losada U, De Aguilera A M, Shaw A, Solano E, Alegre D, Balboa I, Carvalho P, Gaspar J, Borodkina I, Brezinsek S, Douai D, Giroud C, Guillemaut C, Hidalgo C, Huber A, Joffrin E, Loarer T, De La Luna E, Manzanares A, Militello F, De Pablos L and Wiesen S 2020 Impact of divertor configuration on recycling neutral fluxes for ITER-like wall in JET H-mode plasmas *Plasma Phys. Control. Fusion* **62**

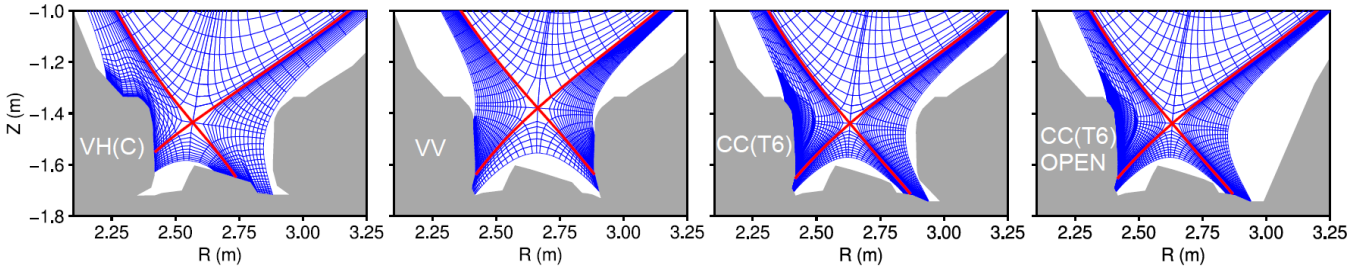

Figure 1: EDGE2D grids corresponding to the VH(C), VV, CC(T6) and CC(T6)-open divertor configurations. The CC(T6) configuration is a compromise in attempting to model the CC configuration by shifting the strike points towards the HFS affording a sufficiently large e-folding width to resolve the SOL upstream density and target particle flux profiles without modifications to the divertor baffle geometry. Note, EIRENE grid outside of the EDGE2D computational domain is not shown.

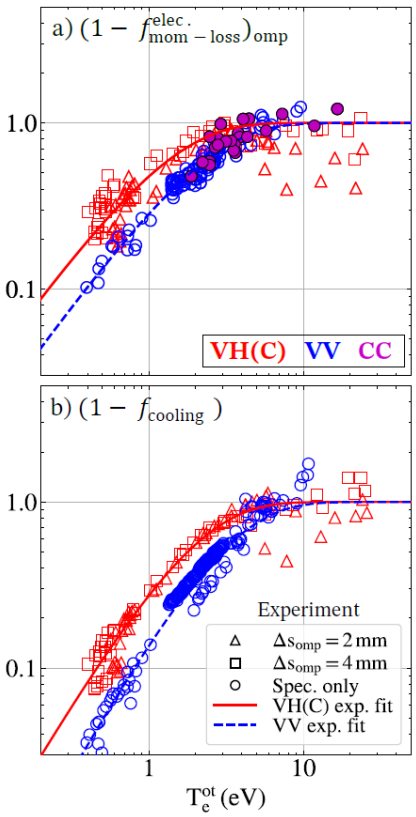

Figure 2: (1-fmom-loss) and (1-fcooling) estimates from L-mode density ramps in VH(C), VV and CC

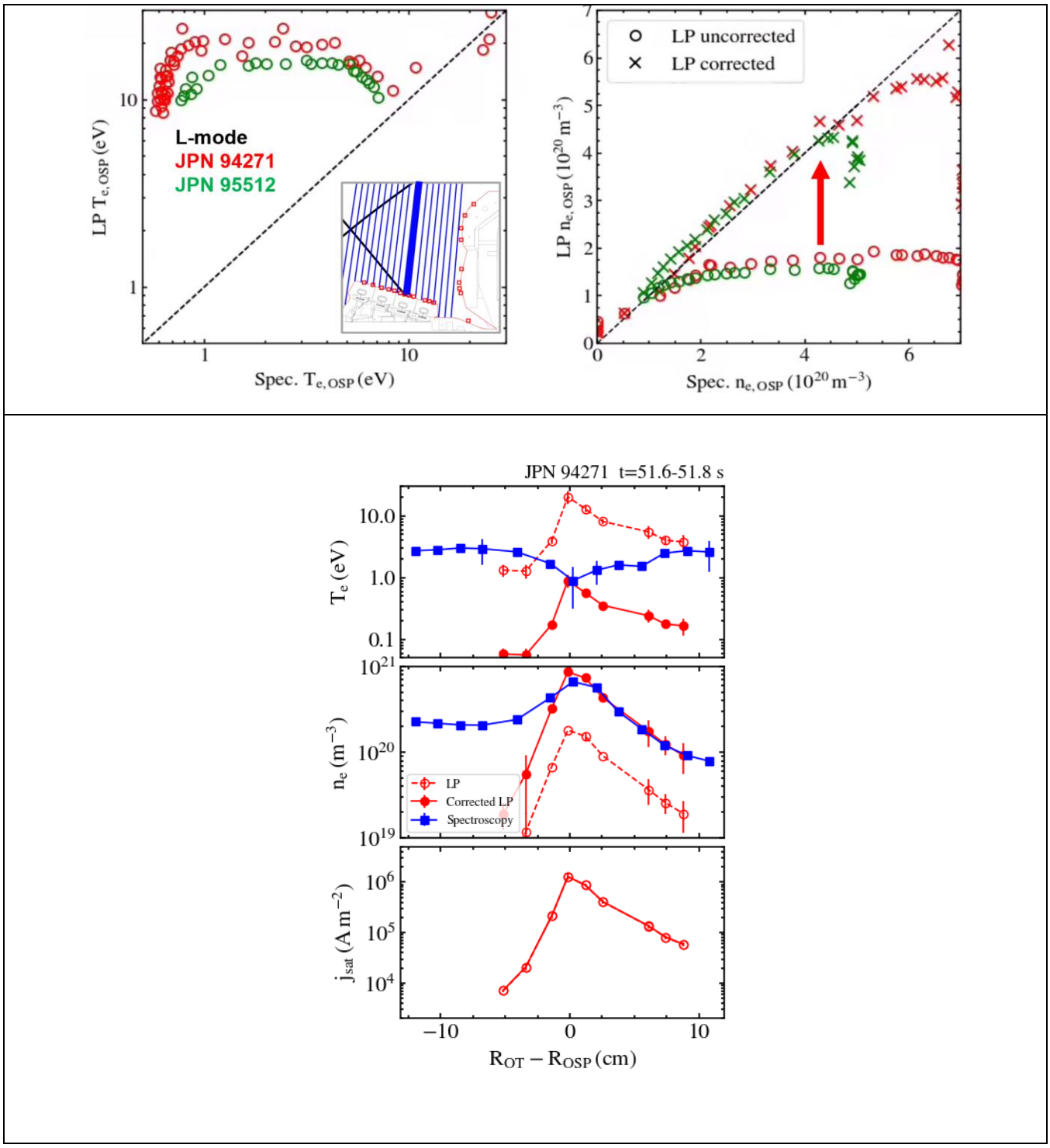

Figure 3: Uncorrected vs. corrected Langmuir probe outer target ne, Te, and jsat profiles.

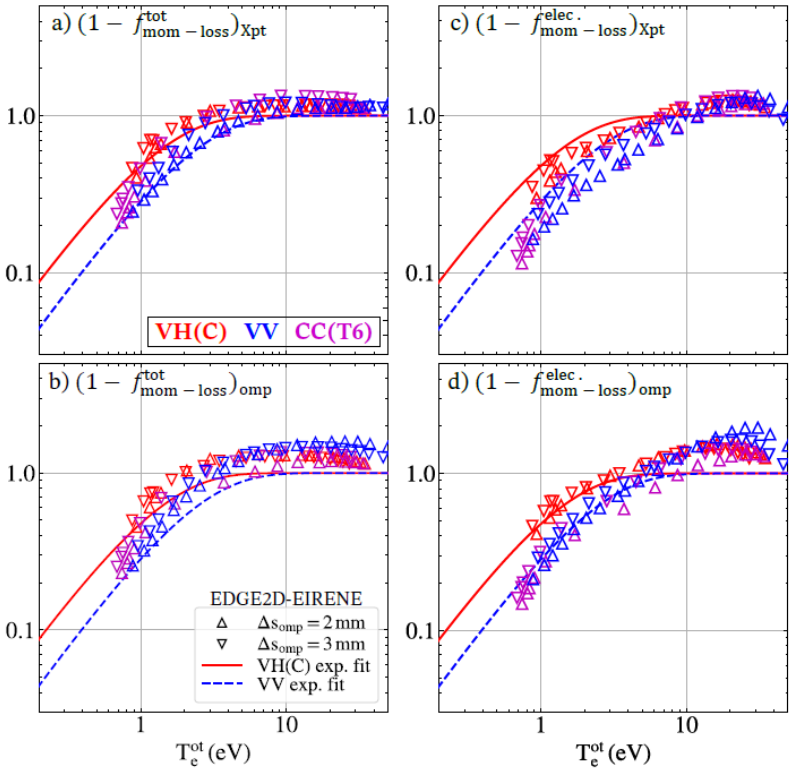

Figure 4: Total and electron pressure loss factors derived from EDGE2D-EIRENE L-mode-like simulations with the upstream location taken at the X-point (a,c) and outer midplane (b,d).

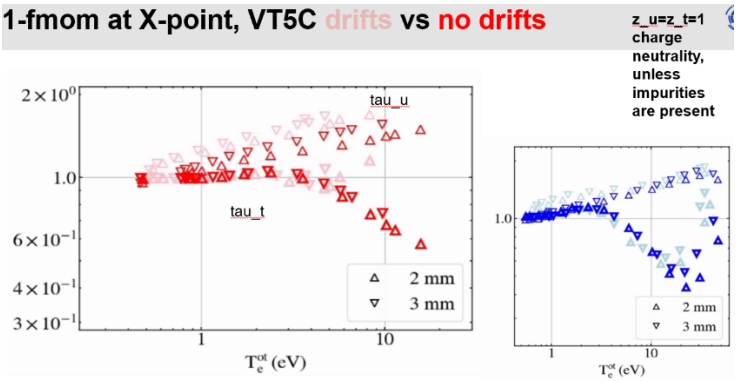

Figure 5: VH(C) and VV $\tau_u=T_{i,u}/T_{e,u}$ and $\tau_t=T_{i,t}/T_{e,t}$ trends from EDGE2D L-mode-like density scan simulations. TODO: replace with publication quality figure.

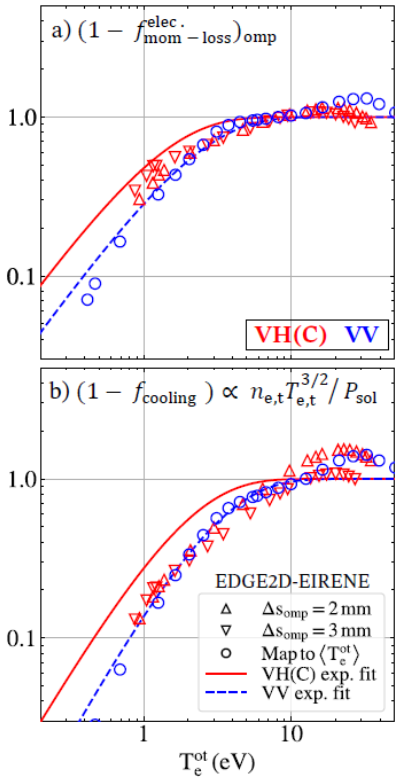

Figure 6: EDGE2D L-mode-like momentum and cooling loss factors consistent with interpretation of experiment data shown in Figure 2.

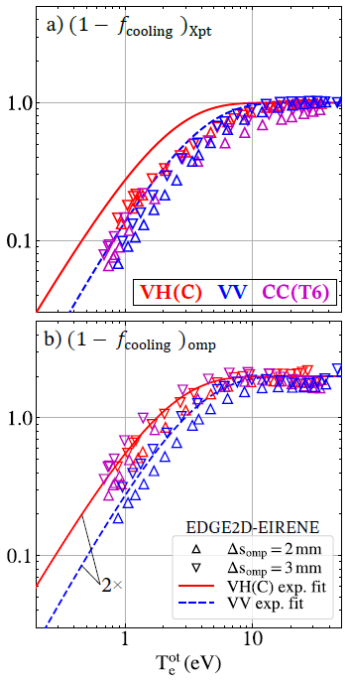

Figure 7: Comparison of EDGE2D L-mode-like cooling loss factors with the upstream location taken at the X-point (a) and outer midplane (b).

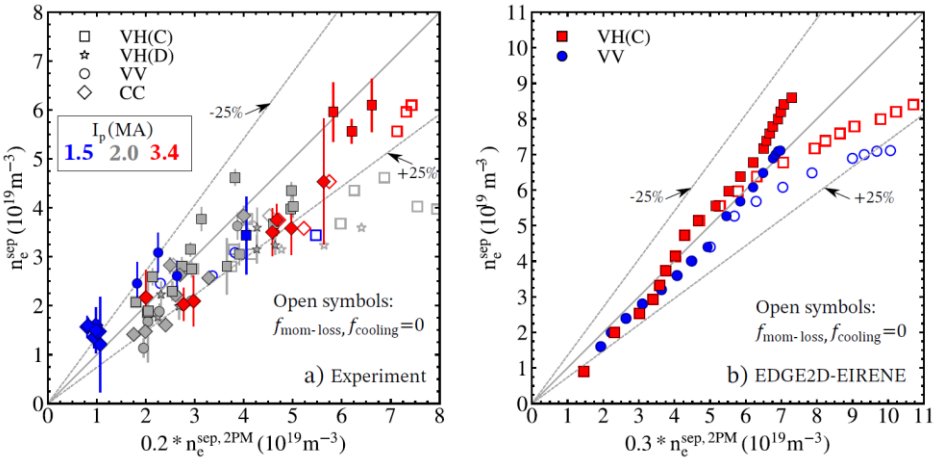

Figure 8: Comparison of measured $n_{e,sep}$ with estimates using the *rev-2PM-simplified* model for the entire H-mode dataset from experiment (a) and the EDGE2D H-mode-like density scans (b). Open symbols correspond to *rev-2PM-simplified* $n_{e,sep}$ estimates in which the momentum and cooling loss factors have been neglected. In (b) the 'measured' $n_{e,sep}$ is estimated using the location along the radial profile corresponding to $T_{e,sep}$ calculated with equation 4 for consistency with experiment.

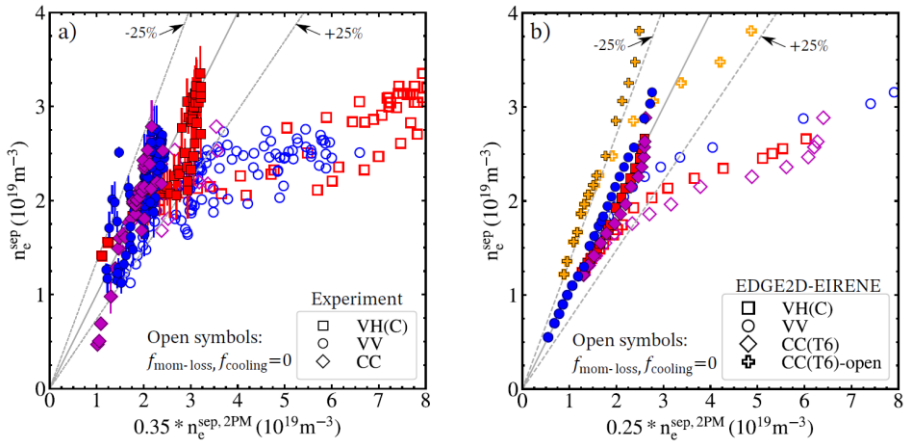

Figure 9: Comparison of measured $n_{e,sep}$ with estimates using the *rev-2PM-simplified* model for the L-mode dataset from experiment (a) and the EDGE2D H-mode-like density scans (b). Open symbols correspond to *rev-2PM-simplified* $n_{e,sep}$ estimates in which the momentum and cooling loss factors have been neglected.

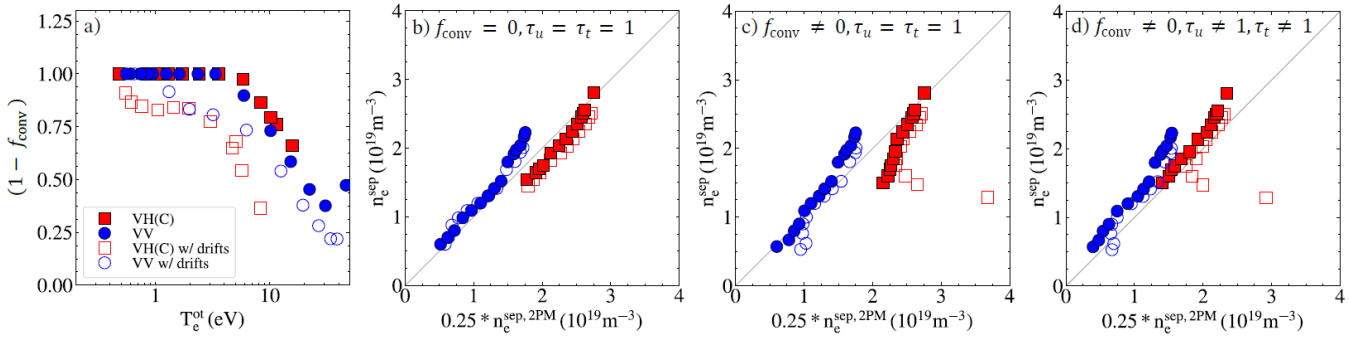

Figure 10: EDGE2D convective fraction as a function of the outer target electron temperature in the third SOL fluxtube from the separatrix with the upstream location taken at the outer midplane (a), rev-2PM $n_{e,sep}$ estimates assuming f_{conv}=0, τ_u=τ_t=1 (b), f_{conv}≠0, τ_u=τ_t=1 (c) and f_{conv}≠0, τ_u≠1, τ_t≠1 with and without drifts.

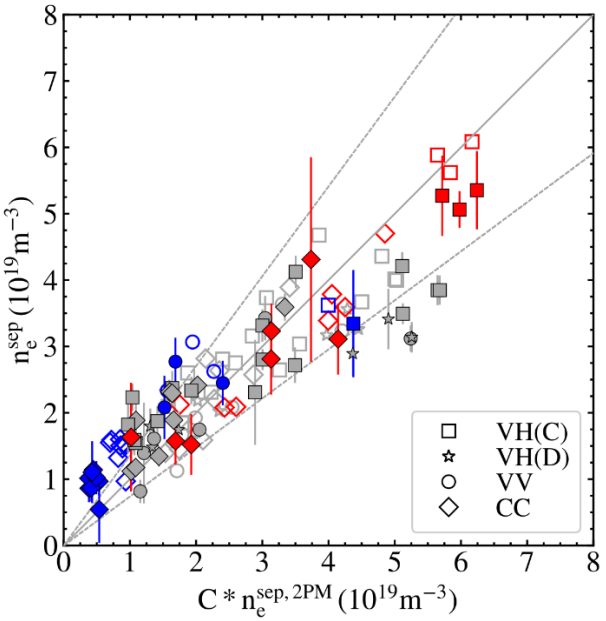

Figure 11: Comparison of measured $n_{e,sep}$ with estimates using the *rev-2PM-simplified* model (open symbols, C=0.2) and *rev-2PM-detailed* model (filled symbols, C=0.3) for the entire H-mode dataset.

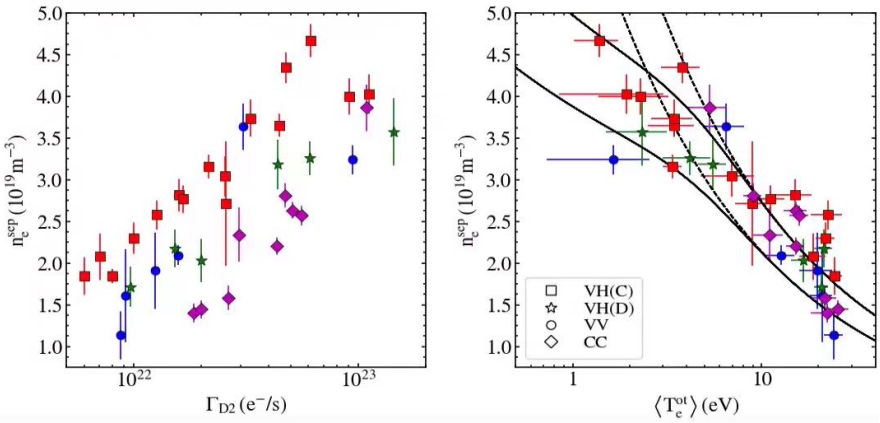

Figure 12: $n_{e,sep}$ vs D_2 fueling rate (a) and $\langle T_{e,ot} \rangle$ (b) for a subset of the H-mode dataset corresponding to 2MA, 2.3 T discharges with P_{sol} in the range 12-17 MW.

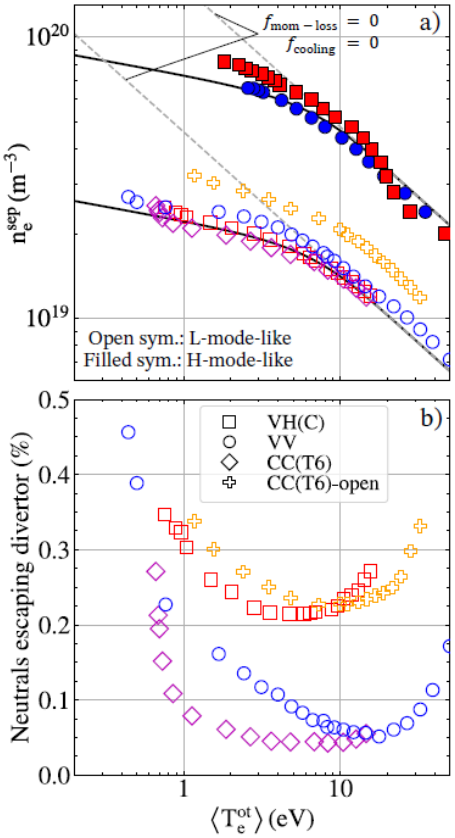

Figure 13: EDGE2D ne,sep vs $\langle T_{e,ot} \rangle$ trends for the L-mode-like (open symbols) and H-mode-like (filled symbols) (a) and percentage of neutrals escaping the divertor vs $\langle T_{e,ot} \rangle$ for the L-mode-like dataset only (b).

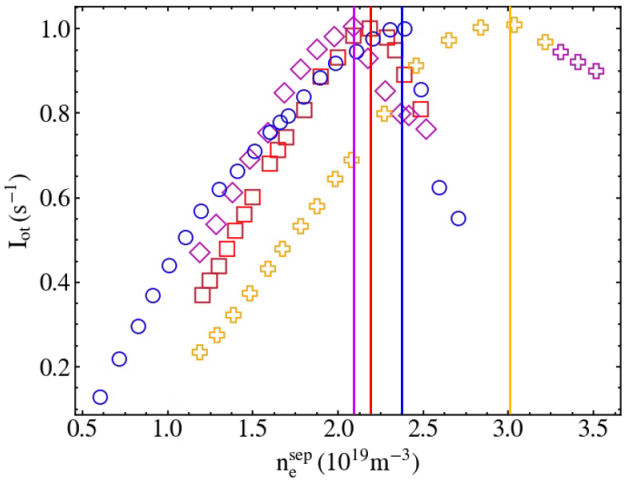

Figure 14: Peak normalized integrated outer target ion current vs $n_{e,sep}$ for the L-mode-like EDGE2D dataset.

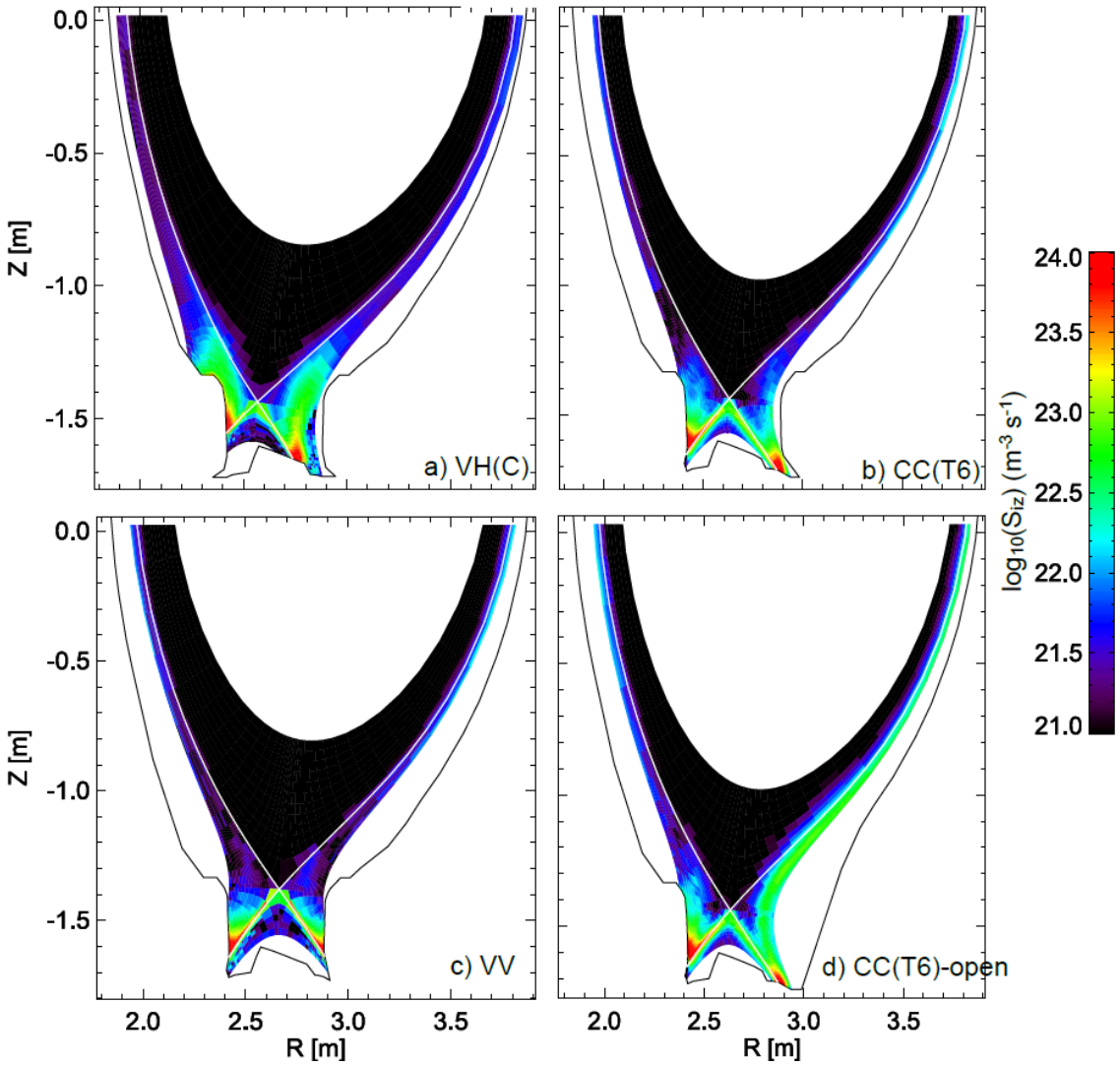

Figure 15: EDGE2D poloidal distribution of total ionization rate with $\langle T_{e,ot} \rangle$=10 eV in the four divertor configuration cases.

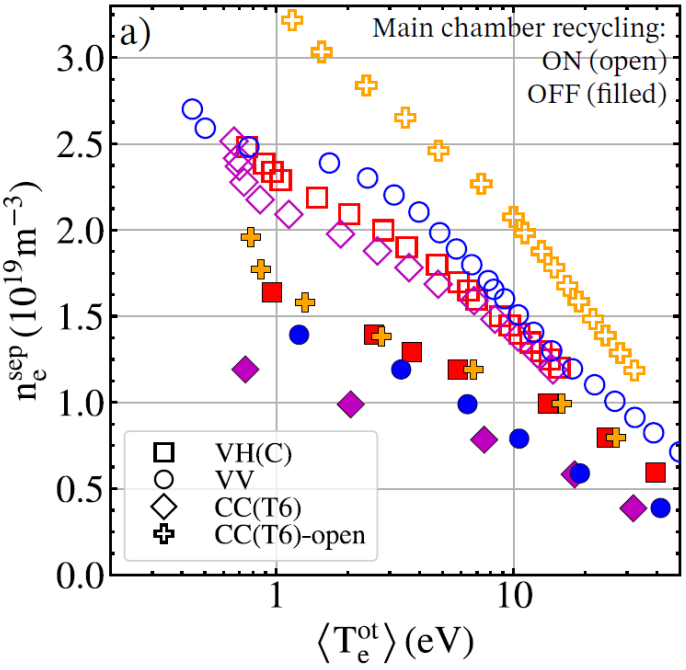

Figure 16: EDGE2D $n_{e,sep}$ vs $\langle T_{e,ot} \rangle$ trends for the L-mode-like simulations with main chamber recycling turned ON (open symbols) and OFF (filled symbols).

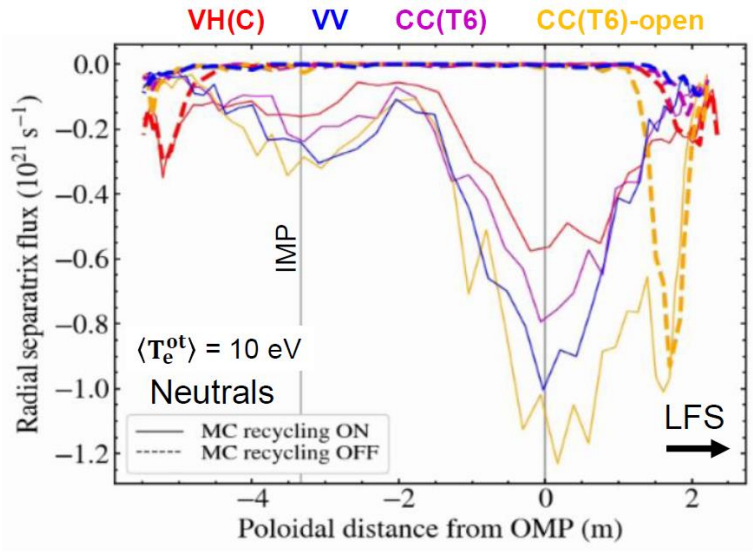

Figure 17: Poloidal profiles of the neutral flux crossing the separatrix for EDGE2D L-mode-like cases at $\langle T_{e,ot} \rangle$=10 with and without main chamber recycling.

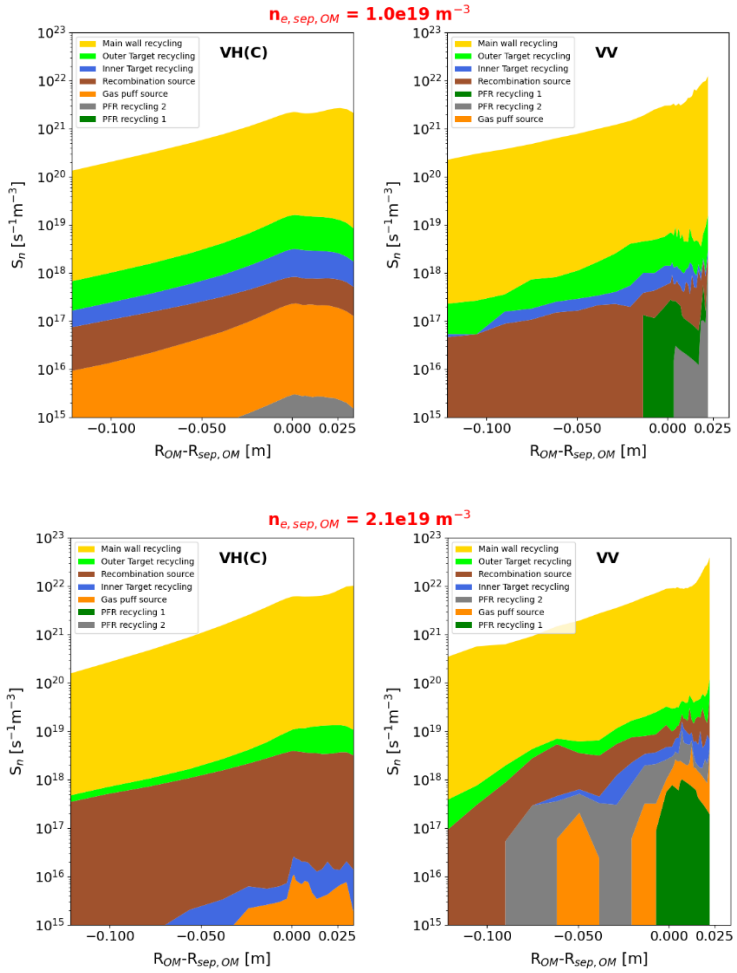

Figure 18: SOLPS-ITER L-mode-like decomposition of the outer midplane ionization radial profile based on the origin of ionized neutrals for low and high $n_{e,sep}$ cases in the VV and VH(C) divertor configurations.

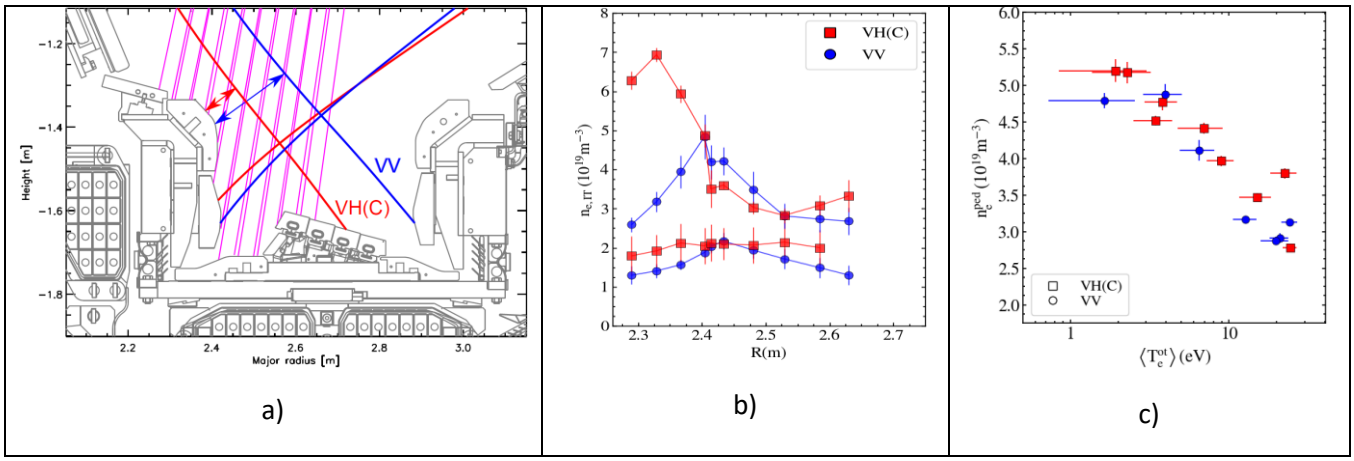

Figure 19: Inner divertor spectroscopic lines of sight and magnetic configurations of the VH(C) and VV geometries showing the relative clearance from the inner divertor baffle to the separatrix (a), electron density profiles inferred from Stark

broadening of the Dδ Balmer line (b) and electron pedestal density vs $\langle T_{e,ot} \rangle$ trends for the 2 MA, 2.3 T, Pnbi=15-16 MW and Picrh=2-3 MW subset of the H-mode dataset.

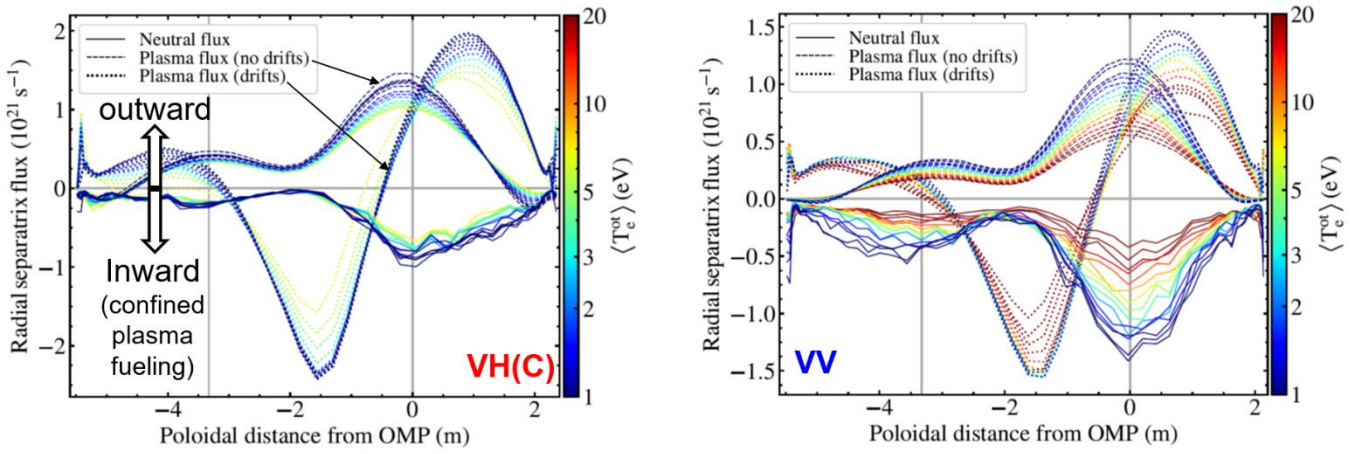

Figure 20: Poloidal profiles of the particle fluxes across the separatrix for the EDGE2D L-mode-like VH(C) and VV simulations. In the cases with drifts, the radial plasma flux is composed of both a diffusive component driven by inverted density gradients and the drift-driven convective flow component. The neutral flux is representative of cases with and without drifts.